Journal
International I J M E of Modern
Engineering
ISSN: 1930-6628
www.ijme.us

INTERNATIONAL JOURNAL OF MODERN ENGINEERING

Fall/Winter 2022
Volume 23, No. 1

The Leading Journal of Engineering, Applied Science and Technology

Industrial

Electronics

Biomedical

Civil

Aerospace

Computer

Electrical

Chemical

Mechanical

ENGINEERING

THE LEADING JOURNAL OF ENGINEERING, APPLIED SCIENCE, AND TECHNOLOGY

Print ISSN: 2157-8052
Online ISSN: 1930-6628

www.ijme.us

www.iajc.org

INTERNATIONAL JOURNAL OF MODERN ENGINEERING

ABOUT IJME:

- IJME was established in 2000 and is the first and official flagship journal of the International Association of Journal and Conferences (IAJC).
- IJME is a high-quality, independent journal steered by a distinguished board of directors and supported by an international review board representing many well-known universities, colleges and corporations in the U.S. and abroad.
- IJME has an impact factor of **3.00**, placing it among the top 100 engineering journals worldwide, and is the #1 visited engineering journal website (according to the National Science Digital Library).

OTHER IAJC JOURNALS:

- The International Journal of Engineering Research and Innovation (IJERI)
  For more information visit www.ijeri.org
- The Technology Interface International Journal (TIIJ).
  For more information visit www.tiij.org

IJME SUBMISSIONS:

- Manuscripts should be sent electronically to the manuscript editor, Dr. Philip Weinsier, at philipw@bgsu.edu.

  For submission guidelines visit
  www.ijme.us/submissions

TO JOIN THE REVIEW BOARD:

- Contact the chair of the International Review Board, Dr. Philip Weinsier, at philipw@bgsu.edu.

  For more information visit
  www.ijme.us/ijme_editorial.htm

INDEXING ORGANIZATIONS:

- IJME is currently indexed by 22 agencies. For a complete listing, please visit us at www.ijme.us.

Contact us:

Mark Rajai, Ph.D.

Editor-in-Chief
California State University-Northridge
College of Engineering and Computer Science
Room: JD 4510
Northridge, CA 91330
Office: (818) 677-5003
Email: mrajai@csun.edu

www.tiij.org

www.ijeri.org

INTERNATIONAL JOURNAL OF MODERN ENGINEERING

The INTERNATIONAL JOURNAL OF MODERN ENGINEERING (IJME) is an independent, not-for-profit publication, which aims to provide the engineering community with a resource and forum for scholarly expression and reflection.

IJME is published twice annually (fall and spring issues) and includes peer-reviewed research articles, editorials, and commentary that contribute to our understanding of the issues, problems, and research associated with engineering and related fields. The journal encourages the submission of manuscripts from private, public, and academic sectors. The views expressed are those of the authors and do not necessarily reflect the opinions of the IJME editors.

EDITORIAL OFFICE:

Mark Rajai, Ph.D.
Editor-in-Chief
Office: (818) 677-2167
Email: ijmeeditor@iajc.org
Dept. of Manufacturing Systems Engineering & Management
California State University-Northridge
18111 Nordhoff Street
Northridge, CA 91330-8332

THE INTERNATIONAL JOURNAL OF MODERN ENGINEERING EDITORS

TABLE OF CONTENTS

In This Issue (p.29)
Hydrogen Storage, Atomic Disorder, Metal Borides, Borophenes, Corrosion Resistance, and Superconductivity.

Philip Weinsier, IJME Manuscript Editor

According to the U.S. Department of Energy, "developing safe, reliable, compact, and cost-effective hydrogen storage technologies is one of the most technically challenging barriers to the widespread use of hydrogen as a form of energy." Current approaches to storing hydrogen include the physical storage of compressed hydrogen gas in high-pressure tanks, the physical storage of cryogenic hydrogen in insulated tanks (cooled to -253°C), storage in advanced materials—such as within the structure or on the surface of certain materials—and storage in the form of chemical compounds that undergo a chemical reaction to release hydrogen.

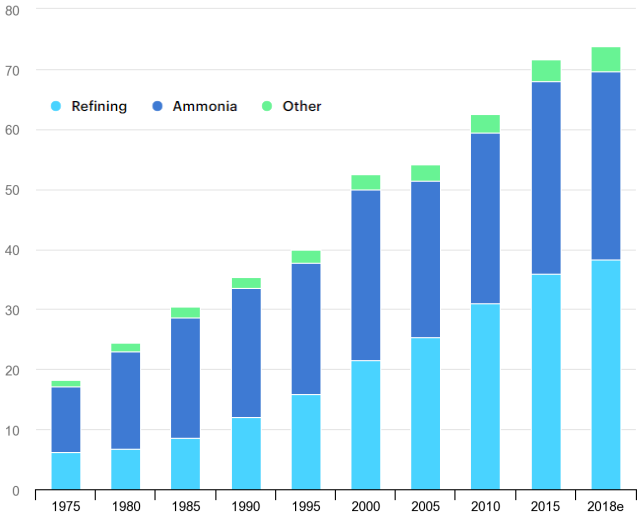

IEA, Global demand for pure hydrogen, 1975-2018, IEA, Paris https://www.iea.org/data-and-statistics/charts/global-demand-for-pure-hydrogen-1975-2018
IEA. License: CC BY 4.0

Scientists are also investigating metal hydrides, adsorbent materials, and chemical hydrides that may offer greater potential for hydrogen storage. Hydrogen storage in materials offers great promise, but additional research on the mechanism of hydrogen storage in materials under practical operating conditions is needed. Additional factors demanding attention include storage capacity, uptake and release of hydrogen, management of heat during refueling, cost, and lifecycle impacts. In a report by Anne M. Stark [*Disorder in Surface Materials Key to Better Hydrogen Storage*, November 4, 2021] of the Lawrence Livermore National Laboratory (LLNL) (Livermore, California), the U.S. Department of Energy and the National Nuclear Security Agency have found that atomic disorder in certain boron-based hydrogen storage systems can potentially improve the rate of hydrogen uptake. She states that borophenes—a single-layer variant of metal borides—are believed to have a regular arrangement of atoms. In many cases, however, LLNL researchers have shown that these atoms dynamically become disordered; a surprise, insofar as most solid-state surfaces typically do not behave in this manner. But while surprising, the researchers found that such disorder provides for different local properties for each atomic site.

Disordered boron surface structure of magnesium diboride probed by atomistic modeling.

The point is that some of these sites can make dissociation of hydrogen molecules easier, which in turn is expected to accelerate activation of the material during hydrogen storage. Moreover, this characteristic also has applications for superconductivity, electrocatalysis, optoelectronics, and as coatings for thermal and corrosion resistance. Brandon Wood—leader of the LLNL team on materials-based hydrogen storage—notes that this capability could be used for custom-tuning surface functionality for faster energy storage and conversion.

Please refer to the article in this issue of IJME on page 29 for an in-depth analysis of hydrogen storage.

Editorial Review Board Members

Mohammed Abdallah	State University of New York (NY)
Paul Akangah	North Carolina A&T State University (NC)
Shah Alam	Texas A&M University-Kingsville (TX)
Nasser Alaraje	Michigan Tech (MI)
Ali Alavizadeh	Purdue University Northwest (IN)
Lawal Anka	Zamfara AC Development (NIGERIA)
Jahangir Ansari	Virginia State University (VA)
Sanjay Bagali	Acharya Institute of Technology (INDIA)
Kevin Berisso	Ohio University (OH)
Pankaj Bhambri	Guru Nanak Dev Engineering (INDIA)
Sylvia Bhattacharya	Kennesaw State University (GA)
Monique Bracken	University of Arkansas Fort Smith (AR)
Tamer Breakah	Ball State University (IN)
Michelle Brodke	Bowling Green State University (OH)
Shaobiao Cai	Penn State University (PA)
Rajab Challoo	Texas A&M University Kingsville (TX)
Isaac Chang	Illinois State University (IL)
Shu-Hui (Susan) Chang	Iowa State University (IA)
Rigoberto Chinchilla	Eastern Illinois University (IL)
Phil Cochrane	Indiana State University (IN)
Curtis Cohenour	Ohio University (OH)
Emily Crawford	Claflin University (SC)
Dongyang (Sunny)Deng	North Carolina A&T State University (NC)
Z.T. Deng	Alabama A&M University (AL)
Sagar Deshpande	Ferris State University (MI)
Marilyn Dyrud	Oregon Institute of Technology (OR)
Mehran Elahi	Elizabeth City State University (NC)
Ahmed Elsawy	Tennessee Technological University (TN)
Cindy English	Millersville University (PA)
Ignatius Fomunung	University of Tennessee Chattanooga (TN)
Ahmed Gawad	Zagazig University (EGYPT)
Hamed Guendouz	Yahia Farès University (ALGERIA)
Kevin Hall	Western Illinois University (IL)
Mohsen Hamidi	Utah Valley University (UT)
Mamoon Hammad	Abu Dhabi University (UAE)
Gene Harding	Purdue Polytechnic (IN)
Bernd Haupt	Penn State University (PA)
Youcef Himri	Safety Engineer in Sonelgaz (ALGERIA)
Delowar Hossain	City University of New York (NY)
Xiaobing Hou	Central Connecticut State University (CT)
Shelton Houston	University of Louisiana Lafayette (LA)
Ying Huang	North Dakota State University (ND)
Christian Bock-Hyeng	North Carolina A&T University (NC)
Pete Hylton	Indiana University Purdue (IN)
John Irwin	Michigan Tech (MI)
Toqeer Israr	Eastern Illinois University (IL)
Sudershan Jetley	Bowling Green State University (OH)
Alex Johnson	Millersville University (PA)
Rex Kanu	Purdue Polytechnic (IN)
Reza Karim	North Dakota State University (ND)
Manish Kewalramani	Abu Dhabi University (UAE)
Tae-Hoon Kim	Purdue University Northwest (IN)
Chris Kluse	Bowling Green State University (OH)
Doug Koch	Southeast Missouri State University (MO)
Mohan Krishna	Vidyavardhaka College of Eng. (INDIA)
Resmi Krishnankuttyrema	Bowling Green State University (OH)
Zaki Kuruppalil	Ohio University (OH)
Shiyoung Lee	Penn State University Berks (PA)
Soo-Yen (Samson) Lee	Central Michigan University (MI)
Chao Li	Florida A&M University (FL)
Jiliang Li	Purdue University Northwest (IN)
Zhaochao Li	Morehead State University (KY)
Dale Litwhiler	Penn State University (PA)
Mani Manivannan	ARUP Corporation
G.H. Massiha	University of Louisiana (LA)
Thomas McDonald	University of Southern Indiana (IN)
David Melton	Eastern Illinois University (IL)
Shokoufeh Mirzaei	Cal State Poly Pomona (CA)
Kay Rand Morgan	iCloud.com
Sam Mryyan	Excelsior College (NY)
Jessica Murphy	Jackson State University (MS)
Rungun Nathan	Penn State Berks (PA)
Arun Nambiar	California State University Fresno (CA)
Aurenice Oliveira	Michigan Tech (MI)
Troy Ollison	University of Central Missouri (MO)
Reynaldo Pablo	Purdue Fort Wayne (IN)
Basile Panoutsopoulos	Community College of Rhode Island (RI)
Shahera Patel	Sardar Patel University (INDIA)
Thongchai Phairoh	Virginia State University (VA)
Huyu Qu	Broadcom Corporation
Desire Rasolomampionona	Warsaw University of Tech (POLAND)
Michael Reynolds	University of West Florida (FL)
Nina Robson	California State University-Fullerton (CA)
Marla Rogers	Fastboot Mobile, LLC
Dale Rowe	Brigham Young University (UT)
Karen Ruggles	DeSales University (PA)
Anca Sala	Baker College (MI)
Alex Sergeyev	Michigan Technological University (MI)
Mehdi Shabaninejad	Zagros Oil and Gas Company (IRAN)
Hiral Shah	St. Cloud State University (MN)
Mojtaba Shivaie	Shahrood University of Technology (IRAN)
Musibau Shofoluwe	North Carolina A&T State University (NC)
Jiahui Song	Wentworth Institute of Technology (MA)
Carl Spezia	Southern Illinois University (IL)
Michelle Surerus	Ohio University (OH)
Harold Terano	Camarines Sur Polytechnic (PHILIPPINES)
Sanjay Tewari	Missouri University of Science &Techn (MO)
Vassilios Tzouanas	University of Houston Downtown (TX)
Jeff Ulmer	University of Central Missouri (MO)
Abraham Walton	University of South Florida Polytechnic (FL)
Haoyu Wang	Central Connecticut State University (CT)
Jyhwen Wang	Texas A&M University (TX)
Boonsap Witchayangkoon	Thammasat University (THAILAND)
Shuju Wu	Central Connecticut State University (CT)
Baijian "Justin" Yang	Purdue University (IN)
Eunice Yang	University of Pittsburgh Johnstown (PA)
Xiaoli (Lucy) Yang	Purdue University Northwest (IN)
Hao Yi	Chongqing University (CHINA)
Faruk Yildiz	Sam Houston State University (TX)
Yuqiu You	Ohio University (OH)
Hong Yu	Fitchburg State University (MA)
Pao-Chiang Yuan	Jackson State University (MS)
Jinwen Zhu	Missouri Western State University (MO)

Control System for Bio-inspired Cuttlefish Fin Locomotion for an Autonomous Underwater Vehicle

Kendra Kim, Arizona State University; Sangram Redkar, Arizona State University

Abstract

By utilizing a fixed-point dynamical analysis with applied statistical methods for further development of bio-inspired cuttlefish fin locomotion, underwater aquatic surveillance for exploration and security and safety missions can be accomplished with autonomous underwater vehicles (AUV). Monitoring services that can be performed with a fishlike drone take into account several factors, such as environmental impact and scientific and business concerns, while preserving ocean resources. Using a regression analysis, the authors examined the relationship between current and depth. This analysis revealed the influence of depth on ocean currents. The ideal system should provide a low-cost, low-maintenance, high-endurance, and agile sensor platform to feed into an intelligent control system. Most aquatic dynamical models do not incorporate buoyancy acting on the system and work with an undulating fin with a simple sinusoidal variation. This current review of the dynamical analysis did include the buoyancy factor. In this study, the authors focused on the fluid-structure interaction of the wave as it moved through the water, the fin's forward motion, and the AUV's buoyancy properties. This was based on statistical confirmation of depth impact to current flow through which the AUV would navigate as well as confirmation of neglecting buoyancy only when the density of the cuttlefish was much more significant than the water.

Introduction

In the review of swimming behaviors, developments in Lighthill's (1971) theory and results from Wu's theory were used to identify areas of opportunity for developing a novel solution. In a design of propulsion technology of the BCF mode, Chowdhury, Prasad, Kumar, Kumar, and Panda (2011) performed an undulation simulation of a fish tail. In that study, the authors proved that the swimming style of a fishtail was efficient over large distances and produced impressive speeds. The system is further explained below, along with developments on Lighthill's (1971) theory. In the study of the braking performance of a biomimetic squid, various braking strategies were tested in terms of stopping ability and the forces acting on the controlled stage. The sizeable negative thrust produced by oppositely directed waves allowed for a short stopping distance and time. Therefore, under complex underwater conditions, the undulating fin propulsion system can effectively perform braking (Rahman, Sugimori, Miki, Yamamoto, Sanada & Toda, 2013). Development of innovative materials can be used for new actuators, such as piezoelectric, ion-conducting polymer metal composite, and shape memory allow (SMA). Wang, Wang, and Li (2011) analyzed actuated SMA wires for propulsive thrust and propulsive efficiency.

This study only included moving forward based on passing waves along the vehicle's body and did not include propulsion as a means of motion. The median paired fin locomotion fish has two types of pectoral swimming behaviors. The first is undulatory locomotion; a wave-like pattern studied for many years. The second is oscillatory locomotion, which is less commonly studied, based on a review of the literature. This movement involves undulatory waves propagated downward from the fish's anterior to posterior. This literature review explored both types of locomotion/swimming maneuvers and mechanisms typically evaluated via experimental evidence and mathematical models. The shape of not only the fins but also the body of the cuttlefish-inspired robot was also considered.

Swimming Behaviors

Two primary swimming behaviors are undulatory locomotion and oscillatory locomotion. Undulatory swimming in fish is principally based on Lighthill's (1960) Elongated Body Theory and Wu's Waving Plate Theory (Singh & Pedley, 2008). Table 1 presents the general notations used for Lighthill's and Wu's equations.

Table 1. The notation used in the Lighthill- and Wu-developed equations.

M	Bending moment distribution
m_b	Mass distribution along the body (i.e., mass per unit length)
L	Lift on the body
ω	Angular frequency of imposed body-wave
ρ	Fluid density

The elongated body theory concludes that a wave that increases the body's amplitude is laterally symmetric in order to enable forward motion. In response to this wave, the fish's body is shaped to minimize the lateral recoil from the movement. The undulatory swimming mode has longitudinal effects of flow separation that Lighthill addressed in a proposed combination of resistive/reactive force theory (Lighthill, 1960). Equation 1 shows how Lighthill's lateral

motion takes the general form of an arbitrary continuous function of x and time t. This equation utilizes the boundaries of the continuous function, where x is within the range of full body length from almost null to full range noted as b.

$$y = h(x,t), 0 < x < b \tag{1}$$

This arbitrary continuous function allows the flow to be the sum of the steady flow around a straight fin and results in the displacements, $h(x,t)$. Equation 2 represents each cross-sectional move with lateral velocity relative to the free stream:

$$\omega = \frac{\partial h}{\partial t} + U\frac{\partial h}{\partial x} \tag{2}$$

This velocity is used to determine the rate of change of momentum of the fluid passing to obtain the work rate by a fish's transverse motion. The work dependent on the tail conditions can be translated to thrust using Equation 3:

$$\bar{P} = \frac{1}{2}m(l)\left[\left(\frac{\partial h}{\partial t}\right)^2 + U^2\left(\frac{\partial h}{\partial x}\right)^2\right]_{x=b} \tag{3}$$

The model of steady-state swimming proposed by Lighthill (1971) required that the rate of change of the lateral moment equal the resultant of the lateral forces and the rate of change of angular momentum about the y-axis equal to the moment of lateral forces about the fixed axis. Further development extended to the slender body theory, where rough approximations can be determined, and Lighthill developed the large amplitude elongated body theory. Based on the following three principles, the instantaneous force on the fish is shown in Equation 4:

$$(P,Q) = \left[m\omega\left(\frac{\partial z}{\partial t},\frac{\partial x}{\partial t}\right) - \frac{1}{2}m\omega^2\left(\frac{\partial x}{\partial a},\frac{\partial z}{\partial a}\right)\right]_{a=0} - \frac{d}{dt}\int_0^1 m\omega\left(-\frac{\partial z}{\partial a},\frac{\partial x}{\partial a}\right)da \tag{4}$$

Principle 1
Water momentum near any fish sections is perpendicular to the backbone with a magnitude of velocity in that direction.

Principle 2
Within a volume of a fish's boundary at each instant, the thrust can be determined by considering the rate of change in momentum.

Principle 3
Pressures generated by motions within the plane and the action of the results are to be taken into account, with the transfer of motion contributing to the momentum balance. In the instantaneous force equation developed by Lighthill, the motion occurs in the xz-plane where a is along the backbone of the fish and $a = 0$ is at the tail. Thus, the mean thrust can be found only in terms of the fish's tail. The recoil is minimized by having an anterior body portion with a cross-sectional depth larger than the tail fin. There is an opportunity for further development, because the requirement of small curvature does not address the starts and turns of fish locomotion. The assumptions involving large lateral deformation and curvature do not address unsteady maneuvers.

This opportunity for addressing the assumptions is to have a realistic representation of environmental circumstances. Without a fundamental understanding of the control system, the applications of the AUV are limited. Expanding these assumptions to include the requirements of curvature will allow AUVs to maneuver in both starting motion and managing turns. In the current state, the AUV is only managed at a level of maintainability once the motion has reached equilibrium. The unsteady maneuvers are not addressed based on how the fin is considered an infinitely thin plate of uniform density hydrodynamically. Due to the symmetry on the xz-plane and the xy-plane, the only breaking from the deformation is on the xy-plane. Assumptions of large lateral deformations suggest a force against the body in only the xy-plane that accounts for the translation along the y-axis but does not address the rotation about the z-axis.

Environmental Conditions

In addition to swimming behaviors, the control system required a consideration of environmental conditions that can be estimated with the distribution parameters identified from the residual plot. The CORREL function expresses the coefficient of the two arrays. This function results in the east current having a -0.038 relationship to depth. Figure 1 shows the current values across a depth sample from 2 to 10. At a lower depth, the current's magnitudes are higher and lower; however, as the depth increases, the current values come closer to zero. Due to the trendline decreasing and the current values coming closer to zero, another review of the current at lower depths was considered. Evaluations of greater depths will assist in the unmanned underwater vehicle application, because the department of defense would need to be capable of having control at a variety of depths. Therefore, evaluating different depths will afford a more practical application.

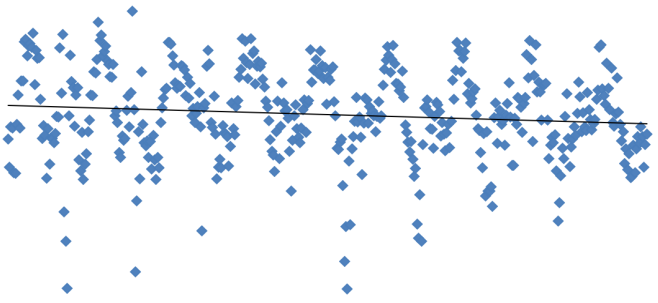

Figure 1. East ocean current versus depth from 2-10.

Figure 2 shows the ocean current from depth samples of 11 to 22. Opposite to the review from the depth trend line (2–10), increased depth has a positive slope, due to the currents being driven by the temperature gradients and density. Density-driven forces and gravity contribute to the fluctuation, as shown on the right side of the graph. The other consideration was that the temperatures were cold and, therefore, caused the density to increase. To verify this theory, the ocean currents were evaluated in a different direction, North. The evaluation at different directions was expected to show an opposite trend line, due to the wind direction affecting the current at lower depth samples and buoyancy requirements.

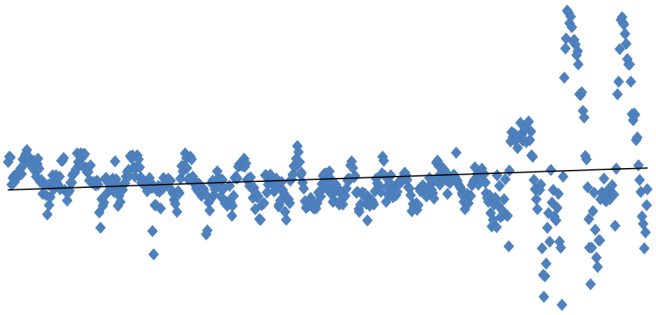

Figure 2. East ocean current versus depth from 11-22.

Figure 3 shows that the current had higher variability as ocean depth increased. The east ocean current had a higher variability, ranging from roughly -60 to 80, whereas the north current range was from roughly -20 to 80. The actual depth for the current range was not as predicted, nor was it linear. The predicted values included a number of outliers and a centralized gathering of current variability from -20 to 20. This shows that the east current had not an increased range of current but a standard current, which means that the residual plot for the east current was expected to have a centralized current. The output summary review shown in Table 2 includes a regression model analysis, and ANOVA details are considered in Equation 5. The simple linear regression model starts with the study of multiple R. The multiple R is the correlation coefficient that shows that the positive relationship was moderate. If this value were one, then the relationship would be nominal. The coefficient of determination indicates that the depth of the current explains 10% of the variation of the current around the mean. Therefore, 10% of the values fit the model. In addition to only having one x variable, there were over 1000 observations in the sample.

The second part of the output is the comparison, where the sum of squares is divided into individual components—the review of the ANOVA, including the sum of squares, regression MS, Residual MS, overall F test for the null hypothesis, and Significant F. The last section of the output summary exposed specific information about the components; in this case, the east and north currents. In addition to the p-value for the hypothesis test, the lower boundary for the confidence interval was the lower 95%, and the upper boundary for the confidence interval was the upper 95%. The most valuable part of this was determining the linear regression equation. This was the y = slope * x + intercept, as given by Equation 5:

$$y = 11.02 - \text{EastCurrent} * 0.01 + \text{NorthCurrent} * 0.15 \quad (5)$$

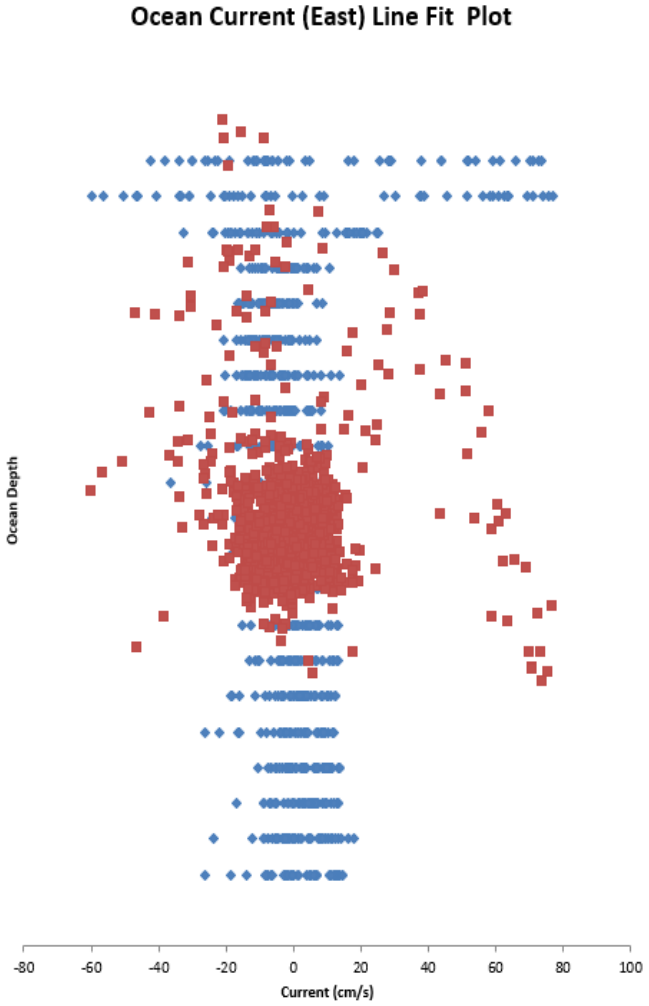

Figure 3. East ocean current line fit plot.

Table 2. Output summary of regression statistics evaluating north currents.

Multiple R	0.325793
R Square	0.106141
Adjusted R Square	0.104362
Standard Error	5.733469
Observations	1008

The degree of freedom is the sum of squares divided by the mean of squares. Since there are 1008 observations, the sum of squares of the residual was adjusted to equal 1005 based on the regression fixed values. The df(regression) equals the number of predictor variables. The df(residual) is the sample size minus the number of parameters being estimated. With parameter tests using alpha = 5%, the two-tail distribution of 2.5% is the critical value. This distribution is used when the p-value is less than alpha, and the confidence interval does not contain the hypothesized mean and is considered significant. When the parameter is close to being less than alpha, it is borderline significant. When the p-value is greater than alpha, there is a risk, meaning it is the least significant parameter. And, when the p-value is less than alpha, this is significant, and the zero values are the most significant. The 95% confidence interval for both parameters was 1.96 from the t-table. Therefore, the intercept and the north current were significant. When the p-value is greater than alpha, there is a risk, which means it is the least significant parameter, the east current.

Buoyancy Fixed-Point Analysis

After reviewing the swimming behaviors and evaluating the environmental conditions, the cuttlefish dynamics model utilized the variables in Table 3 to analyze buoyancy.

Table 3. The notation used in buoyancy fixed-point analysis equations.

A	Amplitude of undulation
k	Spatial frequency
w	Temporal frequency
M	Mass of cuttlefish
V_g	Volume of cuttlefish
D	Drag force
Rho	Density of fluid
Rho_c	Density of cuttlefish
U	Stream velocity

Equation 6 shows the wave equation that utilizes spatial frequency, temporal frequency, and the amplitude of undulation.

$$y = A\sin\left(kx - \omega t\right) \tag{6}$$

When applying Newton's 2nd Law to Equation 6, the resulting equations provide the motion, shown in Equations 7 and 8 in terms of the mass of the cuttlefish.

$$M\dot{x} = \frac{\rho A b_m}{kL}\left(\frac{A^2\omega^2}{2} - \frac{U^2A^2k^2}{2}\right) - \frac{1}{2}C_D\rho S\dot{x} \tag{7}$$

$$M\dot{y} = -\rho_c V_g + \rho V_g = \left(\rho - \rho_c\right)V_g \tag{8}$$

Equations 7 and 8 are rewritten as equations of motion as a three-dimensional dynamical system, which is similar to the previous dynamical system except that there is a *y*-component to the motion now due to the weight of the cuttlefish and the buoyant force shown in Equations 9-11 as the amplitude of undulation.

$$\dot{x}_1 = \zeta + \sqrt{\frac{2\rho A b_m}{kLC_D\rho S}\left(\frac{A^2\omega^2}{2} - \frac{U^2A^2k^2}{2}\right)} \tag{9}$$

$$\dot{\zeta} = -\frac{2}{M}\sqrt{\frac{2\rho A b_m C_D\rho S}{kL}\left(\frac{A^2\omega^2}{2} - \frac{U^2A^2k^2}{2}\right)\zeta} \tag{10}$$

$$\dot{u}_y = -\rho_c V_g + \rho V_g \tag{11}$$

The only major shift in this system is that there was a linear growth in the 3rd dimension of this dynamical system, which means that the topological properties were somewhat similar to the previous one. In Equation 12 there is a focus on the *y* velocity stream.

$$U_y = \left(\rho V_g - \rho_c V_g\right)t \tag{12}$$

The eigenvalue analysis of the system yielded three eigenvalues to this system, as expected and shown in Equation 13, where the criteria of Equation 14 are applied.

$$\lambda = 0, -2\sqrt{C_1C_2}, k \tag{13}$$

$$k = \left(\rho - \rho_c\right)V_g \tag{14}$$

Looking at the system's dynamic behavior, there is a clear indication that the system will behave quite similarly in the presence of buoyancy. Therefore, the neglect of buoyancy is only when the density of the cuttlefish is much more significant than water, which is usually not the case. Controlling the volume of water stored in the cuttlefish UUV design should improve the controllability of the cuttlefish, which is very similar to the submarine model. This detail was used in the software simulation that established the incompressible flow.

Software Simulation

Figure 4 shows that the software simulation included a test diagram made up of 12 key aspects. Figure 5 shows that the first method was the development of the fin model. After the fin was developed, the next method was to create a simulation space that included 10x the longest axis of fin, which was 240 mm. This provided the simulation enough room for turbulences and any deviation in the fluid for

confirmation. Therefore, the simulation space was 0.24m. After the simulation, the selection of settings for an incompressible fluid flow provided a realistic application of water flow and neglected density variation. Simulation settings included a turbulence model of k-omega SST, a steady time dependency, and zero passive species. Once the simulation settings were established, the material settings for the water provided a Newtonian viscosity model that provided a 9.338e-7 m^2/s kinematic viscosity and a 997.3 $kg.m^2$ density. The boundary conditions included inlet, outlet, and static walls to support the proper flow through the simulation. The simulation control was set with a 1-second delta time and an end time of 1000s. The mesh region refinement included physics-based meshing, automatic boundary layers, and a hex element core. The speed of the fluid was 0.25m/s with a mesh quality of two non-orthogonal corrections. Residual controls include $1e^{-6}$ absolute tolerances for velocity, pressure, and turb kinetic energy. The solver settings included smooth solver settings for velocity, turb kinetic energy, and specific dissipation.

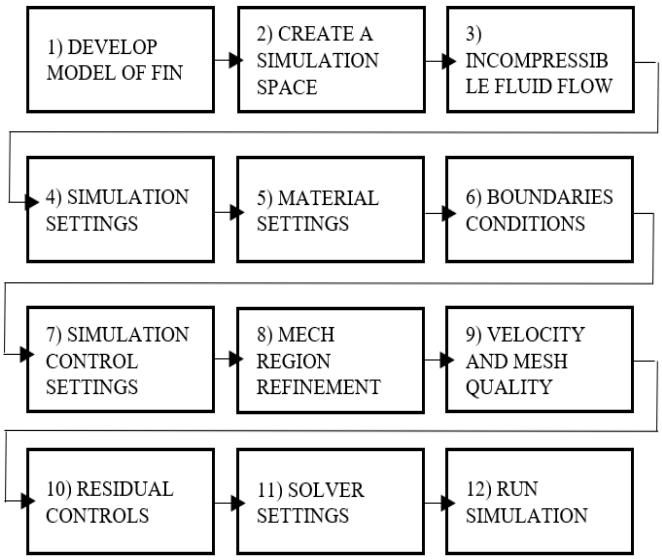

Figure 4. Test diagram for simulation settings and optimization.

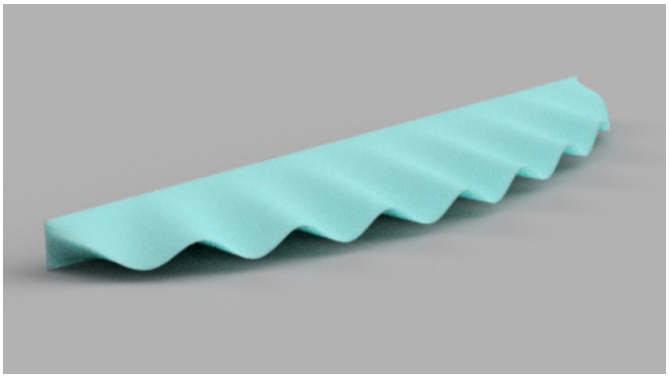

Figure 5. Model of the cuttle fin used in the Simscale simulation.

Simulation and development of the fluid-structure interactions were used through the controller model to showcase stable conditions. It was based on creating a volume of space in which the liquid could move in order to show the fluid-structure interaction as the wave moved through the water. The dynamic condition showcased the interaction, and having an additional representation ensured a more accurate environmental condition evaluation. It was completed with a box that was ten times as large for the fluid to encounter turbulence in order to capture deviations so that they could be accounted for in the simulation. Figure 6 shows that, in order to ensure that the fin was being utilized as expected, the back face did not allow fluid to bypass. Based on the swimming behaviors of the fin, this model was inclusive of the force that is discussed in Lighthill's theory, where thrust is only formed at the tail of a fish. Due to the recoil being reduced, based on having the anterior body portion with a cross-sectional depth larger than the tail fin, the overall system was not simulated. Having the fin mounted in a structure that allowed the full velocity to be directly impacted by the fin showcased the overall structural impact of the cuttle fin design utilizing non-linear motion with the environmental impact captured.

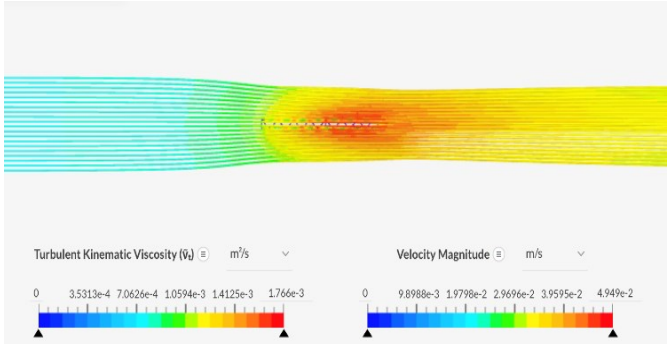

Figure 6. Full fluid flow against the cuttlefish fin.

The simulation utilized an incompressible simulation of flow/fluid, which could simulate the flow of a single fluid. In this simulation, the fluid density variations were negligible and the fluid could be approximated as incompressible. The settings of the material set in water in the simulation model were a Newtonian viscosity model with a kinematic viscosity of 9.338e-7 m^2/s and a density of 997.3 kg/m^3. The simulation worked to a global variable in the *x* direction with a velocity of 0.25 m/s. Figure 7 show the impact in the *z* direction of pressure along with viscous and porous forces.

Figure 7 also shows the *z* direction of pressure and viscous and porous moments. As expected in the equations shown in the fixed-point analysis, this was significantly lower than the *x* and *y* coordinate systems but still had consideration upon fluid impact and started to normalize over time. Figure 8 show the impact in the *z* direction of velocity and pressure, emphasizing the importance of buoyancy, as described by Equation 13.

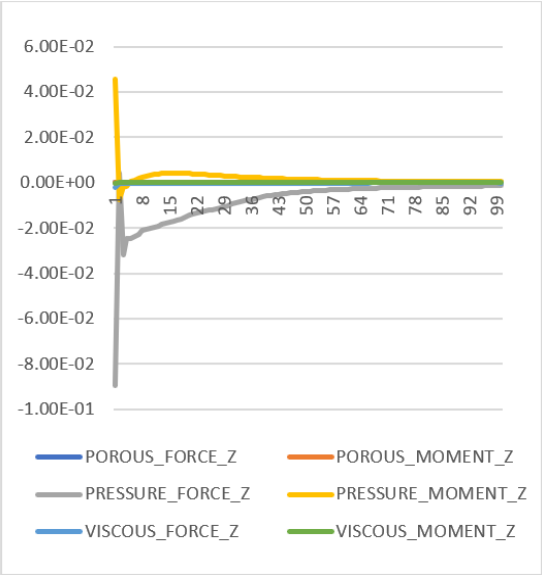

Figure 7. Graphical representation of the simulation with forces and moments.

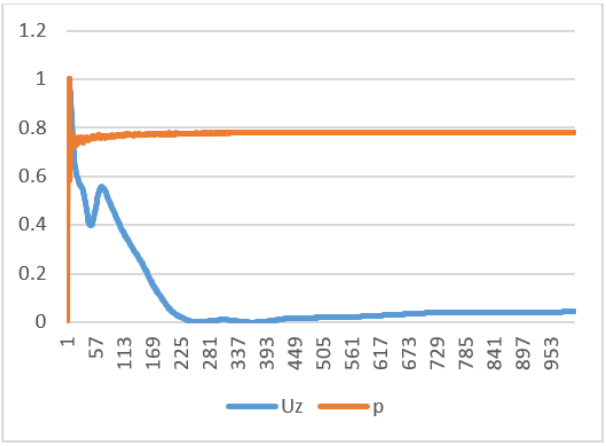

Figure 8. Pressure (p) and velocity (U).

Conclusions

The software simulation confirmed the motion requirements per the environmental analysis, in addition to the fixed-point analysis for buoyancy variables in the cuttlefish fin application. This notes its relevancy to the overall modeling that would include a wave motion within an underwater application. In addition, the non-linear model utilized in this system included an architecture that took into account environmental conditions and fluid-structure interactions that could be used to develop a small-scale model to confirm the overall system architecture. This system had the ability to propel with a forward motion based on the submerged aspects that would be studied to understand the limitations it would have given the environmental conditions of deployment.

References

Chowdhury, A., Prasad, B., Kumar, V., Kumar, D., & Panda, D. (2011). Design, Modeling and Open-loop Control of a BCF Mode Bio-mimetic Robotic Fish. *IEEE International Symposium on Safety, Security, and Rescue Robotics, 6*.

Lighthill, M. (1960). Note on swimming of slender fish. *Journal of Fluid Mechanics, Part 2*, 305-317.

Lighthill. M. (1971). Large-amplitude elongated-body theory of fish locomotion. *Proceedings of Royal Society, 179*, 125-138.

Rahman, M., Sugimori, S., Miki, H., Yamamoto, R., Sanada, Y., & Toda, Y. (2013). Braking Performance of a Biomimetic Squid-Like Underwater Robot. *Laboratory of Hull Form Design, Department of Naval Architecture and Ocean Engineering, Graduate School of Engineering, Osaka University,* 265-273.

Singh, K., & Pedley, T. (2008). Hydrodynamics of Flexible Manoeuvres in Fish. *Physica D: Nonlinear Phenomena, 237*(14-17), 2234-2239, 229.

Wang, Y., Wang, Z., & Li, J. (2011). Initial Design of a Biomimetic Cuttlefish Robot Actuated by SMA Wires. *Third International Conference on Measuring Technology and Mechatronics Automation, 2*, 425-428.

Biographies

KENDRA KIM is an industry professional pursuing a doctorate in systems engineering at Arizona State University. Kendra received her BSE in Electrical Systems Engineering with a secondary focus in robotics from Arizona State University and her MS in Systems Engineering from Arizona State University. She has extensive experience in electronics manufacturing for aerospace, and her interests include complex control systems and bioinspired engineering. Kendra may be reached at klkim@asu.edu

SANGRAM REDKAR is an associate professor at Arizona State University and works in robotics, dynamical systems, and controls. Dr. Redkar may be reached at sredkar@asu.edu

ASSESSMENT OF AFFINE DISTORTION IN FLATBED SCANNERS

Martin P. Jones, Missouri State University; Peter A. Jones, United States Patent and Trademark Office

Abstract

Flatbed scanners have been previously used to measure the dimensions of a variety of objects. Previous studies have attempted to assess the accuracy of such measurements using NIST traceable distortion targets, but each only assessed one scanner model/brand. In this current study, three different scanner models of the same brand were assessed for affine distortion resulting from their scanned images of such a target. At least two scanners of each model were assessed. Also, the potential effects on distortion due to scanning resolution, target position, and operator were explored. The authors found that the remaining overall distortion of the images was about 2.6%, after compensating for affine distortion. Statistical analysis indicated there was no significant effect on this distortion, based on the parameters of operator, target position, and scanning resolution. However, there was a significant effect based on the model and individual scanner used to image the target. In addition, grayscale maps of the remaining distortion were generated and revealed two superimposed patterns: wavelike and columnlike.

Introduction

The common desktop (flatbed) scanner has been used to dimensionally measure a variety of objects. A brief review of such measurements was given by Jones, Callahan, and Bruce (2012), which ranged from rice grain size for food science to wire diameters for the electronics industry (Kee & Ratnam, 2009), where an accuracy of 2.5 mm was claimed. While the common flatbed scanner might not be as accurate for dimensional measurement as other equipment—such as coordinate measuring machines and optical comparators—they are ubiquitous and relatively inexpensive. Previous studies have attempted to assess the dimensional accuracy of flatbed scanners by scanning NIST (National Institute of Science and Technology) traceable calibrated grid distortion targets (Blanco, Fernandez, Noriega, Alvarez, & Valiño, 2020; Jones, Hubbard, & Buyurgan, 2018; Sampson, Peterson, & Lozowski, 2002).

Of these earlier studies, each only assessed one brand/model of scanner and none assessed the same brand from the other studies. Another study did attempt to assess two different scanner brand/models (Elaksher & Ali, 2018). However, the study did not use a NIST traceable target. In this current study, the authors assessed the accuracy of three scanner models from the same brand using a NIST traceable target and modified method developed by Jones et al. (2018).

The original purpose of this study was to determine whether the published method by Jones et al. (2018) could be successfully applied to all three scanner models. While it was found that all three models could be assessed under some combinations of scanning parameters (target position, scanning resolution, etc.), not all combinations could be assessed. Once the method was modified to compensate for the shear distortion inherent in all the scanners, all models under all scanning parameters were able to be assessed as described below.

Overview of Method

Figure 1 shows the overall method used to assess the dimensional accuracy of the scanners.

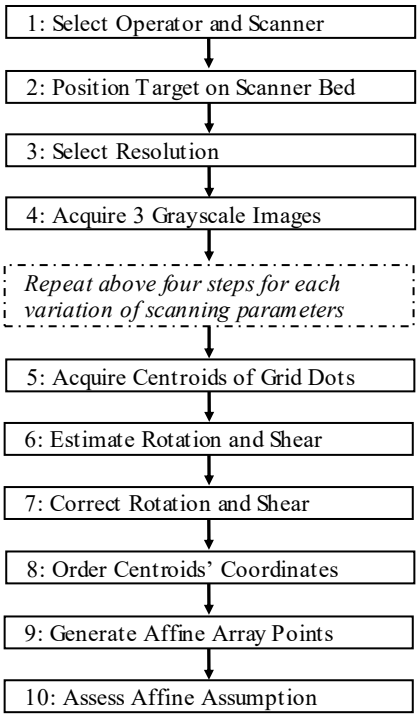

Figure 1. Method for assessing dimensional accuracy.

First, one of two operators selected one of seven desktop scanners. The operator then positioned the distortion grid target in either the top or bottom area of the scanning bed. Then, one of four scanning resolutions was selected via the manufacturer's scanning software. Without changing any of the above parameters, the target was repeatedly scanned three times in order to acquire three separate 8-bit grayscale images of the target's grid of dots.

Steps 1 through 4 were then looped until all combinations of the scanning parameters had been performed: 2 operators, 2 target positions, 4 scanning resolutions, 3 repeated scans, and 7 scanners. This resulted in 336 (2×2×4×3×7) grayscale images. In Step 5, all images were processed in order to acquire the coordinates of the dots' centroids using ImageJ software (National Institutes of Health [NIH], 2022). The coordinates of the dots' centroids were then exported to Microsoft Excel to be further processed and analyzed in Steps 6 through 10. The purpose of Steps 6-8 was to sort the centroids' coordinates into a mathematically addressable order to enable distortion analysis of the scanners. It was observed while initially attempting to order the centroids that a large component of the distortion was affine (especially shear and rotation factors). Therefore, in Step 6, the shear and rotation factors were estimated followed by their correction in Step 7d. This correction enabled the original imaged centroids to be sorted into a mathematically addressable order (Step 8). If the distortion was assumed to be purely affine, theoretical affine array points could be generated that would perfectly predict the location of the imaged dots' centroids. Therefore, in Step 9, theoretical (ideal) affine-distorted target array points were generated that best fit the coordinates of the centroids acquired in Step 5 from the grayscale images. In Step 10, the positions of the imaged centroids were then compared to the best-fit coordinates in order to assess the assumption of affine distortion inherent in the scanners.

Equipment and Scanning Procedure

All seven Hewlett-Packard (HP) brand scanners were purchased new for this current study—two were model N6310, two were model G4050, and three were model G3110. Coincidentally, the G3110 was also used by Elaksher and Ali (2018). Selection of these models was done in consultation with a corporate scanner expert from the Hewlett-Packard company, but no funding (neither cash nor in-kind funding) from HP was received, nor did their expert contribute to the distortion assessment procedure developed in this study. The authors only asked the expert to recommend three scanner models that might exhibit some variation in the image distortion among the models; furthermore, the authors did not ask what the nature or the source of those variations might be, nor did they communicate any data from the present study to the expert. The sole purpose of seeking variation in image distortion among the scanner models was to challenge the applicability of the distortion assessment procedure developed in this study.

Figure 2 shows the two positions at which the distortion target (dot array) was placed onto the scanners' glass bed in order to increase the area of assessment. The depicted *x-y* coordinate system was left-handed, which is common in computer graphics. The distortion target was an Edmund Optics model 62-207 and consisted of a 151 by 151 square grid of 22,801 etched chromium dots, nominally spaced 1.000 mm apart, each being 0.5 mm in diameter, on a soda lime glass substrate. It was NIST traceable within the following tolerances: ±0.001 mm from dot-to-dot centers, ±0.003 mm from grid corner dots, ±0.002 mm for dot diameters, and had an overall accuracy of ±0.002 mm. The square glass substrate was nominally 7.0 inches by 7.0 inches with the dot grid starting about 0.5 inches from the edges of the substrate.

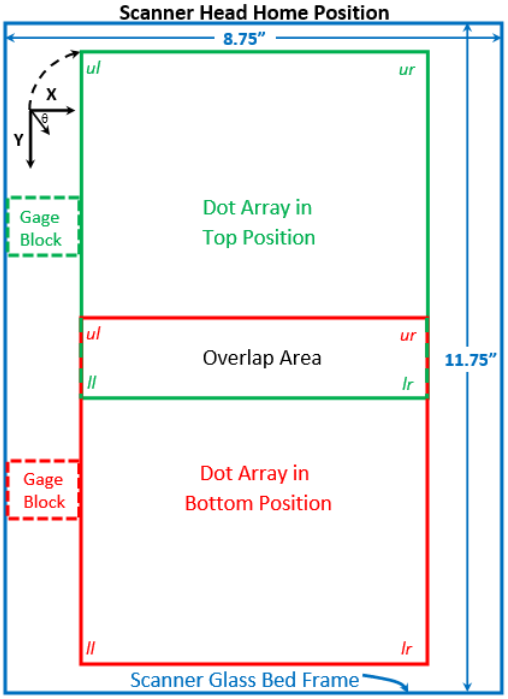

Figure 2. Target placement on the scanning bed.

Two operators (students) were chosen to independently perform aligning and scanning of the target. This was done to provide the reproducibility basis for a gage-repeatability and -reproducibility (gage R&R) measurement analysis of the data. While gage R&R analysis is outside the scope of the present study, possible operator effect on image distortion was considered. A protocol was developed to minimize the variability of aligning the target relative to the scanner bed. As depicted in Figure 2, the target was placed in the top position, flush with the top edge of the target and the top edge of the scanner's plastic frame (near "Home Position"). At the same time, the target was centered in the frame by using a gage block to align it flush with the left edge of the target, which is in contact with the left edge of the frame. A similar procedure was used to place the target in the bottom position. The scanner cover was not closed during scanning of the target in order to avoid stress on the target that might cause damage or a shift in its position.

Once the target was in the top position, it was scanned three successive times at resolutions of 300, 600, 1200, and 2400 dots per inch (dpi) without moving the target in order to obtain 8-bit resolution bitmap images of the dot grid. This

was done to minimize the potential for damage to the target from handling. By scanning three successive times, the repeatability basis for a gage R&R analysis was provided. Again, while gage R&R analysis is outside the scope of the present study, the repeatability aspect of image distortion was considered. The target was then moved to the bottom position and the above procedure repeated.

Image Processing

Images were processed in order to acquire the coordinates of the dots' centroids using ImageJ software, based on a procedure developed by Jones et al. (2018). The software calculates coordinates of the dots' centroids, based on the simple average of the x and y coordinates of all pixels that meet the criteria of being part of a dot. Those criteria consisted of grayscale threshold, circularity, and size requirements. The threshold requirement was set to 180 on a scale of 0 (no reflection) to 256 (total reflection). Thus, any pixel with a value of 180 or less was considered part of a dot. Also, it was required that an imaged dot have a circularity greater than or equal to 0.5 and a range of area in pixels (px) depending on scanning resolution. Table 1 shows the required imaged ranges of areas of a nominal 0.5 mm diameter dot.

Table 1. Criteria for range of area of an imaged target dot.

Resolution (dpi)	Min. Area (px)	Approx. Ideal Area (px)	Max. Area (px)
300	13	27	52
600	54	110	142
1200	218	438	566
2400	500	1753	3000

The threshold criterion was empirically developed to result in an average imaged dot size that approximated the ideal area of a dot. The circularity and size criteria were empirically developed so that all dots on the target were detected, and that no "false" dots were generated. False dots could be generated due to the presence of lint, dust, smudges, etc. on the surface of the target.

Ordering of Centroids

While the ImageJ software was successfully used to locate the estimated centroids of all 22,801 dots on the target, the located centroids were not always output listed in a mathematically addressable order to enable distortion analysis. Paradoxically, it was found that the inherent distortion in the scanned images caused the output listed order of the centroids to vary randomly. It was further found that the distortion was significantly affine. Therefore, to put the centroids in a mathematically addressable order, the centroids were first corrected for some of the affine distortion by applying an inverse rotation and shear transformation to all the coordinates of the centroids. While affine distortion involves translation, scale, rotation, and shear factors, only the correction of the latter two were needed to enable the centroids to be put into a mathematically addressable order. To obtain the inverse rotation and shear transformation, it was first necessary to estimate the numerical shear and rotation factors. The following items describe the procedure for estimating the rotation and shear affine factors and correcting the centroids' coordinates (Steps 6 and 7 in Figure 1).

1. Export the 22,801 centroids' coordinates from ImageJ to Microsoft Excel in their original output listed order: x_i, y_i, where $i = 1$ to 22,801.
2. Calculate the x and y coordinates of the center-of-mass (COM) of all the centroids using Equations 1 and 2:

$$\bar{x} = \frac{\sum_{i=1}^{22,801} x_i}{22,801} \tag{1}$$

$$\bar{y} = \frac{\sum_{i=1}^{22,801} y_i}{22,801} \tag{2}$$

3. Calculate the squared distance of every centroid from the COM using Equation 3:

$$d_i^2 = \left(\bar{x} - x_i\right)^2 \tag{3}$$

4. Order the centroids' coordinates based on their greatest COM squared distance to their smallest (using the Excel "SORT" function).
5. Identify the four corner dots as those centroids with the four greatest squared distances, defined as d_m^2 ($m = 1$ to 4) with corresponding coordinates, x_m, y_m.
6. Identify and define corner dots as the *ul, ur, ll*, and *lr* dots (e.g., *ul* ≡ upper left as shown in Figure 2) using the following logic:
   - If $\bar{x} - x_m > 0$ and $\bar{y} - y_m > 0$, then *ul* dot (upper left) with coordinates ≡ x_{ul}, y_{ul}.
   - If $\bar{x} - x_m < 0$ and $\bar{y} - y_m > 0$, then *ur* dot (upper right) with coordinates ≡ x_{ur}, y_{ur}.
   - If $\bar{x} - x_m > 0$ and $\bar{y} - y_m < 0$, then *ll* dot (lower left) with coordinates ≡ x_{ll}, y_{ll}.
   - If $\bar{x} - x_m < 0$ and $\bar{y} - y_m < 0$, then *lr* dot (lower right) with coordinates ≡ x_{lr}, y_{lr}.
7. Determine if tilt of target, θ, is clockwise (CW) or counterclockwise (CCW), using logic Equations 4 and 5:

$$\text{If } \frac{y_{ul} - y_{ur}}{x_{ul} - x_{ur}} < 0, \text{ then } \theta \text{ is CCW} \tag{4}$$

$$\text{If } \frac{y_{ul}-y_{ur}}{x_{ul}-x_{ur}} > 0, \text{ then } \theta \text{ is CW} \quad (5)$$

8. Calculate the magnitude of θ, based on the angle between the upper left and upper right corners (ul∠ur) using Equation 6:

$$\theta = \left| \tan^{-1}\left[\frac{y_{ul}-y_{ur}}{x_{ul}-x_{ur}} \right] \right| \quad (6)$$

9. Correct tilt of the four corners' coordinates and designate corrected coordinates with prime (′):
   - For CCW tilt, use Equations 7 through 14:

$$x'_{ul} = x_{ul}\cos(\theta) - y_{ul}\sin(\theta) \quad (7)$$

$$y'_{ul} = x_{ul}\sin(\theta) + y_{ul}\cos(\theta) \quad (8)$$

$$x'_{ur} = x_{ur}\cos(\theta) - y_{ur}\sin(\theta) \quad (9)$$

$$y'_{ur} = x_{ur}\sin(\theta) + y_{ur}\cos(\theta) \quad (10)$$

$$x'_{ll} = x_{ll}\cos(\theta) - y_{ll}\sin(\theta) \quad (11)$$

$$y'_{ll} = x_{ll}\sin(\theta) + y_{ll}\cos(\theta) \quad (12)$$

$$x'_{lr} = x_{lr}\cos(\theta) - y_{lr}\sin(\theta) \quad (13)$$

$$y'_{lr} = x_{lr}\sin(\theta) + y_{lr}\cos(\theta) \quad (14)$$

   - For CW tilt, use again Equations 7-14 but make θ negative.

10. Calculate the averages of the x and y shear factors S_x and S_y, respectively, using the corrected four corners in Equations 15 and 16:

$$S_x = \left(\frac{x'_{ll}-x'_{ul}}{y'_{ll}-y'_{ul}} + \frac{x'_{lr}-x'_{ur}}{y'_{lr}-y'_{ur}} \right) / 2 \quad (15)$$

$$S_y = \left(\frac{y'_{ur}-y'_{ul}}{x'_{ur}-x'_{ul}} + \frac{y'_{lr}-y'_{ll}}{x'_{lr}-x'_{ll}} \right) / 2 \quad (16)$$

Note that the tilt had to be corrected prior to calculating the shear factors, as tilt and shear are mathematically similar as representing a slope, which would have resulted in an overestimate of the shear factors.

11. Correct the shear and tilt of all centroids:
   - For CCW tilt correction, use Equations 17 and 18:

$$x'_i = x_i\cos(\theta) - y_i\sin(\theta) \quad (17)$$

$$y'_i = x_i\sin(\theta) + y_i\cos(\theta) \quad (18)$$

where, i = 1 to 22,801.

   - Define the shear-corrected centroid coordinates as x''_i, y''_i. These are related to the tilt-corrected centroid coordinates x'_i, y'_i by Equations 19 and 20:

$$x'_i = x''_i - S_x y''_i \quad (19)$$

$$y'_i = y''_i - S_y x''_i \quad (20)$$

Rearranging the above equation pair results in Equations 21 and 22:

$$x''_i = \left(x'_i - S_x y'_i\right) / \left(1 - S_x S_y\right) \quad (21)$$

$$y''_i = \left(y'_i - S_x x'_i\right) / \left(1 - S_x S_y\right) \quad (22)$$

where, i = 1 to 22,801.

   - For CW tilt, use again Equations 17 through 22, but make θ negative.

The original centroid coordinates were thus able to be put into a mathematically addressable order (Step 8 of Figure 1), as follows. Sort all the above shear/tilt-corrected centroid coordinates pairs (x''_i, y''_i) from Equations 21 and 22, based on increasing size of x''_i-coordinates along with their corresponding original coordinates (x_i, y_i), using the Excel SORT function. Therefore, the first 151 (x''_i, y''_i) pairs are those of the leftmost column of dots, the second 151 (x''_i, y''_i) pairs are those of the next column of dots that are to the right of the first column, etc., ending with the rightmost column of dots' 151 (x''_i, y''_i) pairs. While the coordinate pairs are now in the correct columns, they might not be in the correct order along a given column. To order the 151 pairs within each column, those pairs were sorted based on increasing size of y''_i-coordinates (again using the SORT function). Therefore, the first coordinate pair was at the top

of the leftmost column (upper left) and the last pair (151st) of that column was at the bottom (lower left). This column ordering continued through to the rightmost column where the top (upper right) coordinate pair corresponded to the 22651st dot and the bottom coordinate pair corresponded to the 22,801st dot (lower right). Thus, the original coordinate pairs (x_i, y_i) were simultaneously sorted along with their corresponding shear/tilt-corrected (x_i'', y_i'') pairs in the same addressable order. The addressable order of original centroids was then designated using k as the subscript for (x_k, y_k).

Generation of Ideal Affine Array Points

Estimates of the affine factors were needed to begin to generate an ideal affine array of points. The estimated factors thus far are given by Equations 1 and 2 for translation, Equation 6 for rotation, and Equations 15 and 16 for shear. The final estimated factors for scale are now given by Equations 23 and 24:

$$M_x = \frac{\left[\sqrt{(x_{ul}-x_{ur})^2+(y_{ul}-y_{ur})^2}+\sqrt{(x_{ll}-x_{lr})^2+(y_{ll}-y_{lr})^2}\right]/2}{R(150)/25.4} \quad (23)$$

$$M_y = \frac{\left[\sqrt{(x_{ur}-x_{lr})^2+(y_{ur}-y_{lr})^2}+\sqrt{(x_{ul}-x_{ll})^2+(y_{ul}-y_{ll})^2}\right]/2}{R(150)/25.4} \quad (24)$$

Here, the estimated x and y scale factors, respectively M_x and M_y, were based on the centroid coordinates of the four corner dots. The average of the upper and lower edge lengths was used to calculate the M_x factor, and the average of the left and right edge lengths were used to calculate the M_y scale factor. M denotes magnification. Note that in the above equations, R is the scanning resolution (px/in or dpi), 150 is the ideal length (mm) of an edge of the target grid, and 25.4 is the conversion factor from inches to millimeters. Thus, scale factors less than one would indicate an imaged edge length smaller than the actual length on the target, whereas scale factors greater than one would indicate an imaged edge length bigger than the actual length on the target (i.e., magnified).

Based on Equations 1, 2, 6, 15, 16, 23, and 24, the estimated affine factors are now, $\bar{x}$, $\bar{y}$, θ, S_x, S_y, M_x, and M_y, respectively. The following procedure generated an ideal array of x and y coordinates (in pixels) based on scanning resolution, ideal spacing of target grid dots, and COM. A left-handed coordinate system was used, as is common in computer graphics, to generate the ideal x-coordinates using two nested loops in Visual Basic (VBA) code:

```
X = 0
For c = 1 To 151
For r = 1 To 151
IdealX(r+X) = (R/25.4)(-76 + c) + Xcom
Next r
X = c * 151
Next c
```

where, (-76 + c) represents the x-coordinates of dots (in millimeters) along a column, c.

Here, c = 1 represents the leftmost column of dots and r is the row number in which a dot is located; so that r = 1 is the uppermost row and r = 151 is the lowermost row. Thus, for all 151 dots in the first column (c = 1), the x-coordinate was -75 mm. Continuing to column 2 (c = 2), the x-coordinate was -74 mm for all its 151 dots, etc., until the last column (c = 151), where the x-coordinate was 75 mm for all its 151 dots. The factor R/25.4 was to convert millimeters into pixels, where R was the scanned resolution (pixels per inch) and 25.4 was the conversion of 25.4 mm per inch. Assume the x-coordinate of the center dot of the ideal array was at the x-coordinate of the center-of-mass, obtained from Equation 1 as $\bar{x}$, and was represented by Xcom in the above code. The result of the above nested loops was a one-dimensional ordered array, IdealX(r + X), of the ideal x-coordinates (in pixels) representing the 22,801 centroids of the distortion target's dot grid. This array was defined as X_i, where i = 1 to 22,801.

Similarly, generate Y ideal coordinates using two nested loops in Visual Basic code:

```
Y = 0
For c = 1 To 151
For r = 1 To 151
IdealY(r + Y) = (R/25.4)(76 - r) + Ycom
Next r
Y = c * 151
Next c
```

where, (76 - r) gives the y-coordinates of dots (in millimeters) along row r.

Here, r = 1 represents the topmost row of dots and c is the column number in which a dot is located in the topmost row; where c = 1 represents the leftmost column and c = 151 is the rightmost column. Thus, for all 151 dots in the topmost row (r = 1), the y-coordinate was 75 mm. Continuing to row 2 (r = 2), the y-coordinate was 74 mm for all its 151 dots, etc., until the lowermost row (r = 151), where the y-coordinate was -75 mm for all its 151 dots. Again, the factor R/25.4 was to convert millimeters into pixels, where R was the scanned resolution (pixels per inch) and 25.4 was the conversion of 25.4 mm per inch. It was assumed the y-coordinate of the center dot of the ideal array was at the y-coordinate of the center-of-mass, defined in Equation 2 as $\bar{y}$, and was represented by Ycom in the above code. The result of the above nested loops was a one-dimensional ordered array, IdealY(r + Y), of the ideal y-coordinates (in

pixels) representing the 22,801 centroids of the distortion target's dot grid. This array was defined as Y_i, where i = 1 to 22,801.

The ideal array coordinates, X_i and Y_i, were then sorted as pairs into an addressable ordered array using the following procedure:

All ideal coordinates pairs, (X_i, Y_i), were first sorted based on increasing size of X_i-coordinates using the Excel SORT function. Therefore, the first 151 (X_i, Y_i) pairs would be those of the leftmost column of dots, the second 151 (X_i, Y_i) pairs would be those of the next column of dots to the right of the first column, etc., ending with the rightmost column of dots' 151 (X_i, Y_i) pairs. The ideal coordinate pairs were then sorted into the correct order within each column based on increasing size of Y_i-coordinates using the Excel SORT function. Therefore, the first ideal coordinate pair would be at the top of the leftmost column (upper left) and the last pair (151st) of that column would be at the bottom (lower left). This column ordering continued through to the rightmost column, where the top (upper right) coordinate pair corresponded to the 22651st dot and the bottom coordinate pair corresponded to the 22,801st dot (lower right). The addressable order of ideal array coordinates was then designated using k as the subscript: (X_k, Y_k). Therefore, the addressable order of the ideal array coordinates had the same corresponding addressable order as the imaged centroid coordinates (x_k, y_k):

$$(X_k, Y_k) \triangleq (x_k, y_k), k = 1 \text{ to } 22{,}801$$

Then affine transformed the ideal array coordinates (X_k, Y_k), to best fit the imaged centroid coordinates, (x_k, y_k). These best-fitted ideal coordinates, defined as $(\mathcal{X}_k, \mathcal{Y}_k)$, were calculated by the affine transformation Equations 25 and 26:

$$\mathcal{X}_k = (X_k \cos\phi - Y_k \sin\phi)\mathcal{M}_x + \delta_x + \mathcal{S}_x Y_k \quad (25)$$

$$\mathcal{Y}_k = (X_k \sin\phi + Y_k \cos\phi)\mathcal{M}_y + \delta_y + \mathcal{S}_y X_k \quad (26)$$

where,
k = 1 to 22,801
ϕ is the tilt angle factor of the ideal array
M_x is the scale factor of the ideal array in the x-direction
M_y is the scale factor of the ideal array in the y-direction
δ_x is the translation factor of the ideal array in the x-direction
δ_y is the translation factor of the ideal array in the y-direction
$\mathcal{S}_x$ is the shear factor of the ideal array in the x-direction
$\mathcal{S}_y$ is the shear factor of the ideal array in the y-direction

Note that the tilt part of Equations 25 and 26 assumes that the ideal array will be rotated CW for positive values of ϕ and rotated CCW for negative values of ϕ. The Excel Solver was then used to iterate the above seven affine factors so as to best fit the ideal array to the original imaged centroids. It was found that Solver consistently converged to a solution only when the initial guesses for the seven ideal affine factors were set to the estimated affine factors:

$\phi = \theta$, $\mathcal{M}_x = M_x$, $\mathcal{M}_y = M_y$, $\delta_x = \bar{x}$, $\delta_y = \bar{y}$, $\mathcal{S}_x = S_x$, and $\mathcal{S}_y = S_y$

Solver was then used to find the best fit between the imaged centroids (x_k, y_k) and the affine-transformed ideal array $(\mathcal{X}_k, \mathcal{Y}_k)$, as follows: Solver iterated the affine factors in Equations 25 and 26 until the average distance between (x_k, y_k) and $(\mathcal{X}_k, \mathcal{Y}_k)$ was at a minimum. This average distance, in pixels, was calculated using Equation 27:

$$\bar{D} = \sum_{k=1}^{22{,}801} \left(\sqrt{(\mathcal{X}_k - x_k)^2 + (\mathcal{Y}_k - y_k)^2}\right)/22{,}801 \quad (27)$$

$\bar{D}$ can be converted to millimeters for a given scanning resolution. The "GRG Nonlinear" engine was selected for Solver. However, it was observed that Solver sometimes found the solution minimum using incongruous affine factors with respect to the values of affine factors obtained in the "Ordering of Centroids" section. For example, magnification factors ($\mathcal{M}$) above 1.5 were sometimes arrived at by Solver, which clearly exceeded those estimated during ordering or which could be commonly observed by anyone using a desktop scanner. The other Solver engines of "Simplex LP" and "Evolutionary" also attempted to eliminate the incongruous solutions; however, they proved less successful than the GRG nonlinear engine.

To eliminate incongruous solutions, constraints on affine factors varied by Solver were implemented. Using affine ordering results as a guide, the following constraints to Solver's parameters were then implemented:

$-0.002 < \mathcal{S}_x < 0.005$
$-0.001 < \mathcal{S}_y < 0.004$
$0.99 < \mathcal{M}_x < 1.03$
$0.99 < \mathcal{M}_y < 1.03$

Despite these constraints, it was observed that a few scans had significantly higher average distances, $\bar{D}$, than the vast majority of scans that resulted in $\bar{D} < 0.05$ mm. To force Solver to find more consistent solutions for all scans, the constraint of $\bar{D} < 0.05$ mm was added to Solver's parameters. However, this resulted in Solver not converging to a solution for some scans. In general, nonconvergence can often be caused by the poor choice of initial guesses of factors within the equations to be solved, such as the affine factors in Equations 25 and 26. Of those affine factors, δ_x and δ_y were the simplest mathematically to vary in order to provide alternative initial guesses to Solver. Additional VBA code was added to force Solver to repeat with random shifts (less than 1mm) in initial guesses of δ_x and δ_y if it failed to converge to a solution.

Of 336 scanned images analyzed in this current study, only eight required Solver to be repeated using different initial guesses to achieve convergence. The highest number of different initial guesses required was six. Thus, ideal array points were constructed to individually simulate the affine distortion present in all 336 scanned images of the target. By comparing the ideal array point positions with their corresponding imaged centroids, the affine assumption of distortion was assessed as described below. Furthermore, if there remained underlying patterns of distortion, then they would not be affine.

Results and Discussion: Assessing Affine Assumption of Distortion

The average distance $\overline{D}$ between the ideal array points and the imaged centroids was used to assess the assumption of affine distortion in the 336 scanned images. If all distortion of the images was intrinsically affine, then ideally $\overline{D}$ would be zero. As shown below, $\overline{D}$ was nonzero for all images. There were several major reasons that this would be expected. For example, the ideal array points might be inaccurate due to Solver being set to converge to a minimum $\overline{D}$ rather than set to zero. In practice, setting $\overline{D} = 0$ resulted in nonconvergence. Another possible reason was that ImageJ did not always obtain the true centers of all the chromium dots due to variation of the imaged size and shape of each individual dot.

While the above two reasons could randomly contribute to $\overline{D}$ being nonzero, there may also have been underlying patterns of distortion that were intrinsically nonaffine and which contributed to $\overline{D}$. Note that values of $\overline{D}$ were reported in millimeters to the sixth decimal place, but the authors do not claim this level of measurement precision. Table 2 gives $\overline{D}$ values drawn from groups based on various scanning parameters such as resolution and target position.

JASP statistical software (JASP Team, 2022) was used to analyze the distribution of the 336 $\overline{D}$′s from all scanned images. The mean $\overline{D}$ from all scanned images was 0.025692 mm. Figure 3 shows a Sturges-type histogram of the $\overline{D}$′s distribution, which indicates that it was nonnormal. Furthermore, the Shapiro-Wilk test resulted in $p < 0.01$, indicating nonnormality based on an α level of 0.05. Nonnormality of the $\overline{D}$′s was also indicated when divided into subgroups, based on the scanning parameters of operator, target position, scanning resolution, individual scanner, scanner model, and repeated scans (all other parameters the same). Therefore, nonparametric tests (Mann-Whitney U, Kruskal-Wallis, and Friedman) were used to determine whether there were statistically significant differences in the $\overline{D}$′s within the above subgroups.

Table 3 summarizes the major results of the nonparametric tests of significance in distortion differences among the subgroups.

Table 2. $\overline{D}$ based on each group parameter.

Group Name	$\overline{D}$ (mm)	Group Name	$\overline{D}$ (mm)
All Scans	0.025692	Scan #3	0.026154
Operator A	0.025904	1st Model N6310	0.018995
Operator B	0.025479	2nd Model N6310	0.022367
Top Position	0.026242	1st Model G4050	0.022796
Bottom Position	0.025141	2nd Model G4050	0.023175
300 dpi	0.026546	1st Model G3110	0.025521
600 dpi	0.025494	2nd Model G3110	0.032432
1200 dpi	0.025713	3rd Model G3110	0.034557
2400 dpi	0.025013	Model N6310	0.020681
Scan #1	0.025863	Model G4050	0.022985
Scan #2	0.025058	Model G3110	0.030836

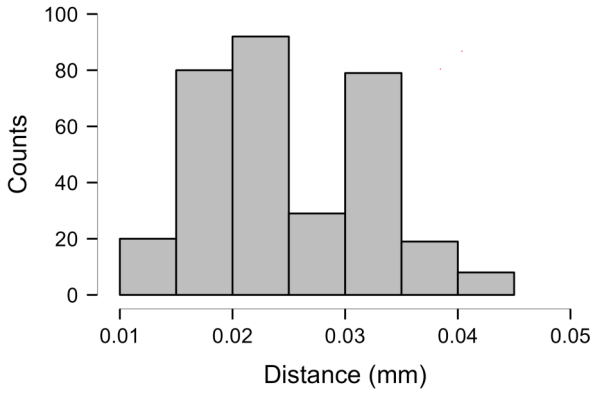

Figure 3. Distribution of $\overline{D}$′s among all scanned images.

Table 3. Major results for tests of significance in distortion differences among subgroups.

Subgroup	Test	p-value	Significant?
Operators	M-W	0.396	No
Target Positions	M-W	0.051	No
Resolutions (dpi)	K-W	0.125	No
Individual Scanners	K-W	0.001	Yes
Model Numbers	K-W	0.001	Yes
Repeated Scans	F	0.42	No

In Table 3, "M-W" indicates Mann-Whitney U, "K-W" indicates Kruskal-Wallis, and "F" indicates Friedman tests. An α level of 0.05 was assumed for each of the tests. The Mann-Whitney U test between the two operators (A and B) resulted in a p-value of 0.396 that, based on an α level of 0.05, indicated no significant difference between operators. This was expected, since operators were given detailed instructions on the careful placement of the target onto the scanner bed. Similarly, the Mann-Whitney U test between the two positions (Top and Bottom) resulted in a p-value of 0.051 that, based on an α level of 0.05, indicated no significant difference between positions. This was not expected, since it was thought that the scanner head might shift or rotate significantly as it moved from top to bottom positions. However, note that the p-value for the positions was much higher than for the operators. This indicated that the effect of position on the mean $\overline{D}$ was possibly greater than the operator effect. Figure 4 displays the mean $\overline{D}$ obtained at each scanning resolution.

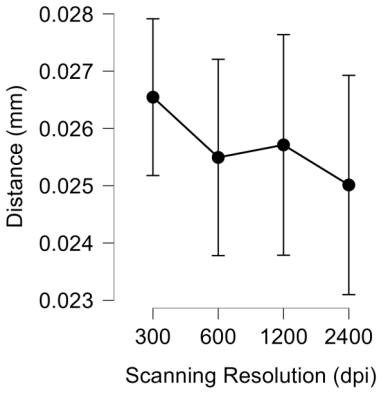

Figure 4. Mean $\overline{D}$ for scanning resolution.

The error bars were based on a 95% confidence interval. Grouping the $\overline{D}$'s according to resolution, the Kruskal-Wallis test resulted in a p-value of 0.125 that, based on an α level of 0.05, indicated no significant difference among the scanning resolutions. This was not expected, since it was thought that higher scanning resolutions would increase the precision in locating the centroids of the imaged dots and, thus, would reduce the differences between them and the ideal array points. However, while resolution was an essential factor in generating the ideal array, it was not allowed to vary in Solver to obtain the minimum $\overline{D}$. This indicated that any increased precision in locating centroids due to increased resolution did not significantly affect $\overline{D}$.

Grouping the $\overline{D}$'s according to their seven corresponding individual scanners, the Kruskal-Wallis test resulted in a p-value of 0.001 that, based on an α level of 0.05, indicated significant differences among the scanners. This was expected, since even small manufacturing variations, such as alignment of the scanner heads during their assembly, might affect the amount and type of image distortion. Additionally, it was expected that the amount and type of distortion would be more affected by the design differences among the three scanner models. Stated differently, it was expected that there would be no significant difference in distortion among scanners of the same model. However, Dunn's post hoc pairwise comparison test on the seven scanners resulted in only the two scanners of model G4050 having a p-value greater than the a level of 0.05, thus indicating no significant difference in distortion. The Dunn's pairwise comparisons also indicated that one of the model N6310 scanners had no significant difference in distortion compared to model G4050. All other pairwise comparisons among the individual scanners indicated significant differences.

Grouping the $\overline{D}$'s according to their three corresponding scanner models, the Kruskal-Wallis test resulted in a p-value of 0.001 that, based on an a level of 0.05, indicated significant differences among the scanner models. This was expected as discussed above. Dunn's post hoc pairwise comparison test between the three scanner models resulted in a p-value of 0.001 for both the model G3110-G4050 and the G3110-G6310 pairs. Based on an a level of 0.05, those two pairs differed significantly. However, the model G4050 -N6310 pairwise comparison resulted in a p-value of 0.05, thus indicating no significant difference.

The final $\overline{D}$ grouping to be discussed were for repeated scans. These were scans where the target was scanned three times in succession for the same position, resolution, operator, and scanner (e.g., all parameters the same). Table 2 lists all scans that were first in succession, regardless of their scanning parameters, were grouped as Scan #1. Similarly, the second and third successive scans were grouped as Scan #2 and Scan #3, respectively. To determine the significance of successive (repeated) scanning on $\overline{D}$, the Friedman repeated measures test was performed and resulted in a p-value of 0.42. Based on an α level of 0.05, this indicated that successive scanning did not significantly affect $\overline{D}$. This was expected, since factors like the target's angle relative to the scanning bed should vary minimally over successive scans.

Regarding the seven factors (ϕ, $\mathcal{M}_x$, $\mathcal{M}_y$, δ_x, δ_y, $\mathcal{S}_x$, $\mathcal{S}_y$) used to generate the ideal array points from Equations 25 and 26, only $\mathcal{M}_x$, $\mathcal{M}_y$, $\mathcal{S}_x$, and $\mathcal{S}_y$ were considered distortions stemming from the scanners, whereas the factors ϕ, δ_x, and δ_y were distortions that stemmed from the relative placement of the target onto the scanners' beds. Since this current study sought to better understand the scanners' distortion factors, the magnification ($\mathcal{M}$) and shear ($\mathcal{S}$) components of the affine distortion were analyzed. The mean M_x and M_y from all 336 images were 1.010531 and 1.007065, respectively. This was interpreted as the images being about 1% larger than the target. While the magnification in the *x*-direction differed only by about 0.3% from that in the *y*-direction, the Mann-Whitney U test indicated that the distributions of those respective magnifications were

significantly different from each other. The means $\mathcal{S}_x$ and $\mathcal{S}_y$ from all 336 images were 0.001429 and 0.000023, respectively. This indicated that the shear in the *x*-direction was over sixty times that of the *y*-direction. In addition, if one compares the *x*-coordinate of an upper right corner dot (UR) to that of a lower right corner dot (LR), the mean $\mathcal{S}_x$ would shift the *x*-coordinate of the LR dot by 0.214 mm to the right of the UR's dot *x*-coordinate. Furthermore, the maximum $\mathcal{S}_x$ result was 0.005000, which would translate similarly into a 0.75 mm shift. Considering that the target's dot centers were nominally spaced 1.000 mm apart, this amount of shear shift in the imaged dots' centroids supports the need to correct the shear (by Equations 19 and 20) to enable the centroids to be put into a mathematically addressable order. Preliminary statistical analysis of the shear distortion was performed based on groups similar to those used above for $\overline{D}$. Discussion of those results and further analysis of the shear distortion will be left to future work.

Patterns of Nonaffine Distortion

As described above, the assumption of affine distortion resulted in a mean $\overline{D}$ of 0 .025692 mm from all 336 scanned images. Based on the nominal 1.000 mm dot spacing on the target, this result could be interpreted as an average error of about 2.6% in the prediction of the locations of the imaged centroids. From another viewpoint, if the estimated factors were used in an inverse transform to correct the affine distortion, there would still be about 2.6% average distortion remaining. A possible contributing source of that error could stem from not optimizing the constraints under which Solver obtained those factors. In addition, perhaps the remaining distortion (nonaffine) could partially stem from the random mechanical, electronic, or reflective variation of the scanner head as it traveled down the scanner bed. This variation might be more systematic than random, such as mechanical periodicity from the head stepper motor drive or from the linear electronic delay of data transfer across the scanner head. If the remaining distortion was significantly from systematic sources, it was conjectured that there might be some patterns of distortion like barrel, perspective, etc., over the scanned area. To visualize any such patterns, distortion maps were created based on the distance, D, between an imaged centroid and its corresponding best-fit ideal array point (similar to Equation 27). Figure 5 shows an example of a distortion map from a model N6310 scanned at 1200 dpi with the target at the top position of the bed.

Each distortion map had 22,801 D values, corresponding to each of the dots on the target. Each D value was assigned a relative 8-bit grayscale value, where the smallest D value was assigned 0 (white) and the largest D value was assigned 255 (black). There seemed to be two dominant patterns in the distortion map of Figure 5. One pattern was wavelike in the *y*-direction (scan head travel) and the other was columnlike across the *x*-direction (scan head). Since the patterns seemed direction-dependent, the distortion data of Figure 5 was divided into its *x* and *y* components, creating two separate distortion maps, as shown in Figures 6 and 7. Figure 6 shows that the *y*-component exhibited the wavelike pattern but not the columnlike pattern; whereas Figure 7 shows that the *x*-component exhibited a columnlike pattern but not a wavelike pattern.

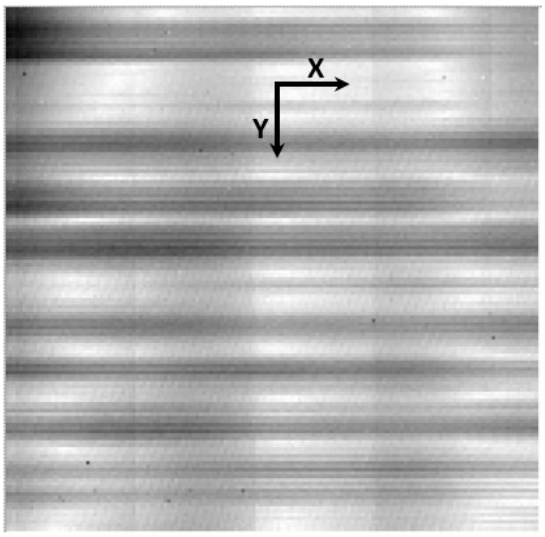

Figure 5. Grayscale map (150 mm by 150 mm) of distances between ideal points and imaged centroids of target dots.

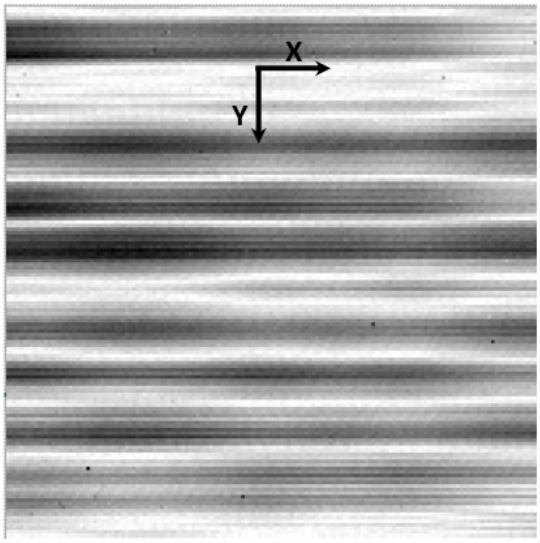

Figure 6. Grayscale map (150 mm by 150 mm) of distances between *y*-coordinates of ideal points and imaged centroids of target dots.

Figures 6 and 7 indicate that the two patterns tend to be independent of each other and, therefore, might arise from separate sources. Future work will be needed to better understand how these patterns vary among the scanners and under different scanning parameters. Some preliminary qualitative observations, however, can be stated within the scope of the present study. All scanners exhibited these

wavelike and columnlike patterns, but the overall patterns seemed to vary more among the different scanner models than within a scanner model. Operator and target position parameters did not appear to affect the overall patterns as much as which scanner model was used. Patterns appeared to be most similar for repeated scans (same parameters). Columnlike patterns seemed to appear more frequently at higher scanning resolutions.

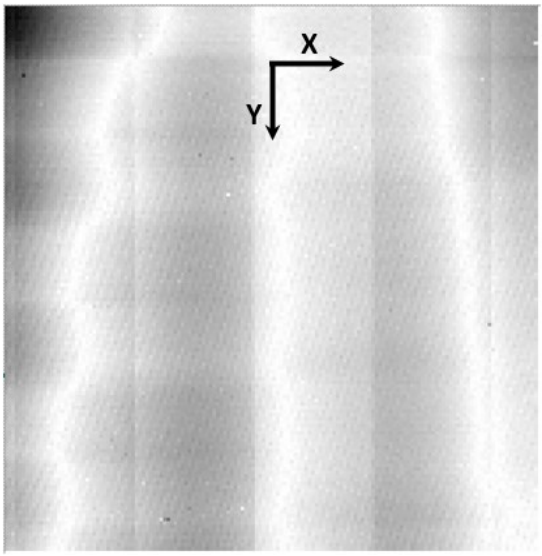

Figure 7. Grayscale map (150 mm by 150 mm) of distances between *x*-coordinates of ideal points and imaged centroids of target dots.

Conclusions

Estimates of the scanners' affine distortion factors were successfully used to order all centroids corresponding to the imaged dots of the target. Affine distortion factors were then iterated to generate an ideal array of points that best fit the corresponding centroids. Average error in distance for all 336 scans, $\overline{D}$, between generated array points and centroids was about 2.6%. The distribution of the $\overline{D}$'s for all scans was nonnormal, thus requiring nonparametric statistical analysis. There were statistically significant differences in $\overline{D}$ when scans were grouped based on some scanning parameters. Grouped by scanner, there were significant differences in the $\overline{D}$'s among the individual scanners. Grouped by scanner model, there were also significant differences in the $\overline{D}$'s among the three scanner models. No statistically significant differences were found in $\overline{D}$'s when grouped by operator, target position, or scan resolution. This indicated that to minimize image distortion, the specific affine factors iteratively obtained from an individual scanner should be used rather than those factors typical of a scanner model. Therefore, to minimize distortion, the authors propose that a target should be imaged by a scanner and then the obtained affine factors used in an inverse affine transformation of all subsequent images from that scanner.

Even with an inverse affine correction, there still was an average of about 2.6% distortion remaining. Distortion maps were created to visualize whether there were patterns to this remaining (underlying) distortion. Preliminarily, these maps revealed two dominant patterns present in the data from all scanners: wavelike in the *y*-direction and columnlike in the *x*-direction. Although the wavelike pattern was similar to that described by Jones et al. (2018), it did not show the columnlike pattern. While these patterns varied from scan to scan, overall patterns seemed to be more consistent (i.e., characteristic) within a given scanner model. Future work will be needed to understand the sources and consistency of these underlying nonaffine patterns in order to further correct image distortion inherent in these scanners.

References

Blanco, D., Fernandez, P., Noriega, A., Alvarez, B. J., & Valiño, G. (2020). Layer contour verification in additive manufacturing by means of commercial flatbed scanners, *Sensors, 20*(1), 1-24.

Elaksher, A. F., & Ali, T. (2018). Geometric calibration of low-cost flatbed scanners for large scale mapping Applications. *Modern Instrumentation*, *7*(2), 11-23.

JASP Team (2022). *JASP* (Version 0.16.3)[Computer software]. https://jasp-stats.org

Jones, M. P., Callahan, R. N., & Bruce, R. D. (2012). Dimensional measurement variation of scanned object using flatbed scanners. *Journal of Technology, Management, and Applied Engineering, 28*(2), 2-12.

Jones, M. P., Hubbard, K. M., & Buyurgan, N. (2018). A simplified algorithm for automated rotation correction of scanned distortion grid targets. *International Journal of Modern Engineering, 19*(1), 35-43.

Kee, C. W., & Ratnam, M. M. (2009). A simple approach to fine wire diameter measurement using a high-resolution flatbed scanner. *International Journal of Advanced Manufacturing Technology, 40*, 940-947.

National Institutes of Health (2022). *ImageJ* (Version 1.53r) [Computer software]. https://imagej.nih.gov/ij/

Sampson, R. D., Peterson, A. E., & Lozowski, E. P. (2002). Photogrammetric calibration of a consumer grade flatbed scanner. *Geomatica, 56*(2), 121-130.

Biographies

MARTIN P. JONES is a professor emeritus in the Technology and Construction Management Department at Missouri State University. Dr. Jones received his BS in physics from the University of Maryland Baltimore County, and MS and PhD in materials science and engineering from the Johns Hopkins University. His research interests include dimensional metrology. Dr. Jones may be reached at MartinJones@MissouriState.edu

PETER A. JONES is a paralegal specialist at the United States Patent and Trademark Office (USPTO) with the Patent Trial and Appeal Board. His contribution to this paper does not represent any endorsement by the USPTO. Mr. Jones received his BS degrees in Chemistry and Philosophy from Missouri State University and his JD from Chicago-Kent College of Law at Illinois Institute of Technology. He is a registered member of the Unites States Patent Bar. His research interests include intellectual property. Mr. Jones may be reached at pjones11@kentlaw.iit.edu

Characterization of Volatile Markers in Electronic Components via Solid-Phase Microextraction and Comprehensive Two-Dimensional Gas Chromatography with Electron Ionization Time-of-Flight Mass Spectrometry (GCxGC/EI-TOF-MS)

Joseph Cacciatore, Purdue University; Petr Vozka, California State University, Los Angeles; Louis Edwards Caceres-Martinez, Purdue University; Ali Daneshkhah, Northwestern University; Mangilal Agarwal, Indiana University and Purdue University Indianapolis; Gozdem Kilaz, Purdue University; Eric Dietz, Purdue University

Abstract

The development of novel non-destructive methodologies for the verification of electronic component authenticity is imperative in reducing the economic and safety risks associated with the use of counterfeited products. Currently, inspection methods rely on a series of electrical and physical tests that usually are labor intensive, destructive, and still not 100% effective, given their dependence on human interpretation. In this paper, the authors present an alternative method using solid-phase microextraction (SPME) and comprehensive two-dimensional gas chromatography with electron ionization time-of-flight mass spectrometry (GCxGC/EI-TOF-MS) to chemically characterize electronic components. The novel approach outlined in this study utilized the high sensitivity of GCxGC/EI-TOF-MS systems to consistently identify more than 300 volatile markers in two different groups of 14-pin, 16-bit microcontrollers and one group of 16 GB microSDs from three different manufacturers. Results showed that the chemical characterization of the electronic components was effective, repeatable, and non-destructive.

The significant volatile markers were found to be dependent on the manufacturer, age, and type of electronic component. Thus, the list of significant volatile markers of each electronic component could potentially serve as a basis for verifying the source of an electronic component. Compared to existing physical verification methods, this novel approach is faster and less ambiguous, and avoids the overlook or false identification of counterfeits. In fact, this methodology could potentially indicate if further inappropriate manipulations have taken place on the component, based on the presence and quantity of 1,3,5-cycloheptatriene, thereby reducing the risk of counterfeit components being installed in electronic systems. Using GCxGC/EI-TOF-MS and SPME techniques may be helpful in reducing the quantity of counterfeit electronic components found in warfare systems used by the United States Department of Defense (DoD), which is especially at risk, due to the rapid aging of deployed systems and a vast span of interconnected logistics supply chains that provide components for installation in such warfare systems.

Introduction

Electronic components are prevalent in many consumer products and throughout most warfare systems utilized by the United States Armed Services. Ensuring that these systems function reliably is mission-critical to the Army, Air Force, Navy, and Marine Corps (Petel, 2014). Thus, there is an incentive for the DoD to ensure that the components and electronic devices used in complex electronic military systems function correctly, even in the most adverse and strenuous environments. This condition represents a huge challenge for DoD, since the failure of electronic components is difficult to predict and usually caused by myriad conditions. However, failure can be significantly prevented (Semiconductor Industry Association SIA, 2011) if the installation of counterfeit parts (i.e., remarked, repackaged, recycled, refurbished, or even cloned devices) are avoided (Mura, Murru & Martines, 2020)

Given the evolving, modern sophisticated counterfeiting techniques, it is pertinent for the DoD to develop an effective method for identifying the authenticity of electronics to ensure national security. Common techniques currently available in the industry for identifying counterfeits include a series of electrical and physical tests that must be performed by highly qualified experts, usually involving multiple analytical techniques. On the one hand, analyzing contact degradation, device parameter distributions, and chip curve trace are recommended practices for evaluating the electrical performance of a component (Ahmadi, Tavousi, Favata, Shahbeigi-Roodposhti, Pelapur & Shahbazmohamadi, 2018) Physical characterization, on the other hand, encompasses the inspection of packaging quality, labeling on the integrated circuits (ICs), and analysis of the structure of the die through simple visual inspection and high-tech imaging techniques such as X-ray, infrared, acoustic microscopy, scanning electron microscopy, and focused ion beams (Chen, Zhang & Zhang, 2014) Neverthe-

less, these methods, especially those based on visual physical assessments, are time consuming, most of them destructive (Hillman, 2011) and still far from being 100% effective, since they rely on human interpretation.

Despite all efforts, the amount of counterfeit electronic devices that have found their way into the DoD supply chain increased from 3868 in 2005 to 9356 in 2008 (U.S. Department of Commerce, 2010) Although this trend decreased in subsequent years, thanks to the creation of the Counterfeit Prevention Policy in 2013, the DoD has been unable to eradicate the issue in full (United States Government Accountability Office, 2016) The introduction and proliferation of counterfeit electronic devices in DoD systems are attributed to two causes: 1) many systems within the DoD are used far beyond their expected end-of-service dates, and 2) the development of the globally integrated economy prevents logistically sourcing products produced solely within the United States (Gansier, Lucyshyn & Rigiliano, 2013) These factors have made it easier for counterfeit products to find their way into the DoD logistics supply chain. According to the Alliance for Gray Market and Counterfeit Abatement, about 100 billion dollars are reportedly lost worldwide by electronic companies every year, due to counterfeited products (Pecht & Tiku, 2006) Analogously, it is estimated that "as many as 15 percent of all spare and replacement semiconductors purchased by the Pentagon are counterfeit" (Semiconductor Industry Association SIA, 2011.

There are four primary sources for electronic components: the original manufacturer, the original manufacturer's authorized distributors, independent distributors or brokers, or aftermarket manufacturers (Sullivan & Wilson, 2017. As a preventative method, the DoD always seeks to purchase components from a "trusted source," which is a source known to produce genuine electronic components. This trusted source is typically the original manufacturer. However, because some systems have been extended far past their end-of-service date, components may have to be purchased from sources other than the original manufacturer because they may no longer manufacture the component (Livingston, 2010) The DoD may be forced to purchase from the original manufacturer's authorized distributors or even independent brokers, who may not be as completely vetted. This less-than-desirable situation creates an opportunity for counterfeit electronic components to find their way into DoD systems, creating a weakness in the Nation's security, as components are not constructed to required specifications or are manufactured with a vulnerability to malicious malware through backdoor applications (Petel, 2014)

Under this perspective, it is imperative that alternative methods be developed to non-invasively and unambiguously determine the fidelity of electronic components such as semiconductors, microcontrollers, and processors used in warfare systems before their actual installation and use (Livingston, 2010) Preliminary alternative approaches to identifying counterfeits include: 1) the analysis of the electromagnetic fingerprint of the IC as a contactless side channel for measuring its transient activity (Huang, Boyer & Ben Dhia, 2015),and 2) the chemical characterization of ICs through flowing atmospheric-pressure (helium plasma) afterglow mass spectrometry (FAPA-MS) complemented with chemometric techniques (Pfeuffer, Caldwell, Shelley, Ray & Hieftje, 2014) Nevertheless, the robustness and complete development of the electromagnetic method (Huang et al., 2015),and the variable response of FAPA-MS to different types of analytes (alkanes, alcohols, aldehydes, ketones, carboxylic acids, and organic peroxides), and the effects of further oxidation processes occurring in the afterglow region are still matters of discussion (Brüggemann, Karu & Hoffmann, 2016).

One-dimensional gas chromatography (GC) coupled with solid-phase microextraction (SPME) is a proven method for identifying trace volatile organic compounds (VOCs) in the headspace surrounding solid and liquid samples of unknown composition. SPME-GC/MS has been used to study the feasibility of canine detection of mass storage devices (DeGreeff, Cerreta & Rispoli, 2017) Additionally, these analytical techniques have been commonly used in chemical forensics for identifying unknown compounds at extremely low concentrations (Brasseur, Dekeirsschieter, Schotsmans, de Koning, Wilson, Haubruge & Focant, 2012; Gordin & Amirav, 2000) Aiming to complement these alternatives, a non-target approach, based on comprehensive two-dimensional gas chromatography with electron ionization time-of-flight mass spectrometry (GCxGC/EI-TOF-MS) and solid-phase microextraction (SPME), is proposed here to characterize the chemical fingerprint of electronic components. GCxGC separates at least an order of magnitude more compounds compared to conventional one-dimensional gas chromatography (GC) (Reddy & Nelson, 2013)

This capability broadens the possibility of studying complex chemical mixtures usually found in forensic (Stadler, Stefanuto, Byer, Brokl, Forbes & Focant, 2012) environmental, fuels, food, fragrances, and biological applications (Prebihalo, Berrier, Freye, Bahaghighat, Moore, Pinkerton & Synovec, 2018) However, to the best of the authors' knowledge, GCxGC has not been used to study volatile markers present in electronic components. Thus, this work was aimed at the development of an alternative and non-destructive method for identifying VOCs in electronics as a potential approach for assessing the authenticity of microcontrollers and micro storage devices in the near future. The results of this study showed that different types of electronic components with different manufacturers, countries of origin, and ages have different chemical signatures, and demonstrated that it is possible to differentiate between equivalent components that differ along with these variables.

Materials and Methods

For this current study, three different types of electronic components were selected for sampling: two types of 14-pin, 16-bit microcontrollers (Microchip Technology Incorporated, 2009; Texas Instruments, 2004) and a 16 GB microSD card (SanDisk, 2019) Thirty replicates of each component type were performed along with 16 controls designed to capture the baseline composition of environmental and instrument VOCs adequately. Controls consisted of one run relative to a column blank, two runs designed to study the natural chemical elution of the SPME fibers, and thirteen runs of the SPME fibers exposed to empty vials. Compounds that were found in more than half of the control group samples were automatically excluded from consideration for possible VOCs of significance in the electronic components. Table 1 details the sample size composition. Once each population was sampled, the chemical signatures of the electronic components were compared to the volatile compounds identified in the controls in order to determine the common and unique VOCs of each group. It is worth mentioning that the comparison with certified counterfeit components was not possible in this current present study, given the uncertainty related to their procurement process.

Table 1. Sample information.

Product classification	14-pin 16-bit Microcontroller	16 GB MicroSD Card	
Manufacturer	Microship Technology	Texas Instruments	SanDisk
Country of Origin	Thailand	Malaysia	China
Date of Manufacture	October 2015	May 2017	2019
Samples Collected	30	30	30

Prior to sampling, 20 mL glass headspace vials were placed in an oven for eight hours to clean the vials of any VOCs remaining from manufacturing. Component samples were removed from the original manufacturer's packaging and placed directly in the cleaned vials. The vials were then purged with nitrogen for 10 seconds to remove ambient environmental VOCs before submersion in a water bath at 70°C. The temperature of 70°C was selected to protect the electronic components from being destroyed during the sampling process. This temperature was within the safe operating temperature defined by the manufacturers (Microchip Technology Incorporated, 2009; SanDisk, 2019; Texas Instruments, 2004) Divinylbenzene/ carboxen/ polydimethylsiloxane (DVB/ CAR/ PDMS) solid-phase microextraction (SPME) fibers were preconditioned at 250°C for ten minutes prior to sampling each day (DeGreeff, Cerreta & Rispoli, 2017). The fibers were manually exposed to the samples within the vial for 50 minutes before being manually injected into the inlet of the GCxGC/EI-TOF-MS, set at 250°C for desorption of the VOCs.

In this study, the authors used GCxGC/EI-TOF-MS. Pegasus GC-HRT 4D (EI) High-Resolution TOF/MS (LECO Corporation, Saint Joseph, MI) with an Agilent 7890B gas chromatograph, a non-moving quad-jet dual-stage thermal modulator cooled with liquid nitrogen, and an Agilent G4513A auto-injector was used for qualitative analysis of the samples. Table 2 shows the chromatographic conditions for GCxGC/EI-TOF-MS. The ion source temperature was set to 250°C and the electron energy was 70 eV. ChromaTOF (Version 1.90.60.0.43266) software was utilized for data collection (with an m/z of 50-1000), processing, and analysis. The signal-to-noise ratio was set to three. Identification of the compounds was achieved by matching the measured mass spectra (similarity value of > 600) with Wiley (2011) and NIST (2011) mass spectral databases. This analysis method was selected in order to yield a broad spectrum of VOCs for consideration.

Table 2. Chromatographic conditions for sample analysis.

Parameter	Description
Columns	Primary: ZB-35HT Phenomenex (60 m × 0.25 mm × 0.25 μm) Secondary: ZB-1HT Phenomenex (1.9 m × 0.25 mm × 0.25 μm)
Carrier gas	UHP helium, 1.20 mL/min
Inlet	Purge time: 60 sec Purge flow: 85 mL/min
Oven Temperature	Isothermal 40°C for 2 min, followed by a linear gradient of 8°C/min to a temperature of 280°C, being held isothermally for 1 min
Modulation Period	2.0 s with a 0.6 s hot pulse time
Temperatures	Inlet: 250°C Transfer line: 250°C

Peak tables generated by individual samples were manually analyzed to generate a list of reliable VOC markers for each sample group tested. For this current study, only compounds that were named using the mass spectral databases listed above were considered. Duplicate named compounds within a given sample were removed from consideration. Furthermore, compounds were required to meet three criteria: 1) they had to be present in at least 25 of the 30 replicates within each sample group, 2) they had to be present in less than half of the control samples, and 3) they had to have reliable retention times. Table 3 shows that, due to instrumental drift, similarly named compounds within sample groups were selected as reliable markers, if they fell within a reliable retention time range.

Results and Discussion

On average, more than 300 compounds were correctly identified for each group, exhibiting the success of the SPME technique and the excellent resolution achieved through GCxGC/EI-TOF-MS. The Microchip Technology microcontroller counted the least (319), while the microSD counted the highest (405) amount of volatile compounds. Inversely, the 14 pin, 16-bit microcontroller manufactured by Microchip Technology exhibited the largest standard deviation (70) among samples, while the microSD counted the lowest (20). The 14-pin, 16-bit microcontroller by Texas Instruments lay in between with 378 VOCs with a standard deviation of 24 compounds. The lower amount of VOCs and higher standard deviation of the microchip developed by Microchip Technology (Thailand) compared to the device manufactured by Texas Instruments (Malaysia) could be attributed to either different origins/manufacturing processes or aging conditions among them—with the last one being 19 months newer. Aging, in fact, has been a key factor previously identified that induced detectable changes in the electromagnetic fingerprint of ICs (Huang et al., 2015)and it is expected to induce changes in the chemical fingerprint as well.

After narrowing down the list of identified VOCs to those unique to each component type, retention time analysis was used to identify the significant VOCs across samples. Table 3 displays the list of significant VOC markers for each sample group that met the required selection criteria, while achieving excellent consistency in terms of retention times. Across the three sample groups, there were two significant VOC markers identified in the Microchip Technology sample group, six in the Texas Instruments sample group, and twenty-one in the SanDisk sample group. These compounds could be considered as the chemical fingerprints of each electronic component and manufacturer representing potential key VOCs to be used for further comparison to counterfeit suspects.

Most VOCs present in the microSD group were found to be around one order of magnitude greater than the VOCs found in either of the microcontroller sample groups. This condition allows identifying the total surface area of the electronic device sampled as a key factor affecting the diffusion rates of VOCs into the headspace during the SPME (Pawliszyn, 2012) The total surface area of components showed that the surface area of the sampled microSDs (380.2 mm^2) was slightly more than twice as large as the total surface area of the sampled microcontrollers (188.4 mm^2). Differences among different ionization efficiencies could also account for the differences in the peak areas among different chemical compounds. However, the difference in surface area, age, and manufacturer of the electronic component were clearly identified as critical factors, when comparing the peak areas for 1,3,5-cycloheptatriene, the only VOC marker identified as significant across all three sample groups. This compound, 1,3,5-cycloheptatriene, is a cycloolefin monomer commonly used as a polymerization retarder in the manufacturing process of cross-linkable resins widely found in electronic components, due to their excellent electrical insulation properties, mechanical characteristics, and heat resistance (Sugawara, 2007).

Based on these findings, further work should focus on quantifying significant VOCs as a function of the aging process under both virgin and expected normal use technical conditions. This mapping, to be unique for each electronic component produced by each manufacturer, could potentially serve as the chemical fingerprint needed for unambiguously identifying counterfeit products present in the DoD logistics supply chain. Given the high resolution and repeatability achieved through SPME and GCxGC/EI-TOF-MS techniques, it is reasonable to expect that any use or modification by means of relabeling, repackaging, or refurbishing (Sood, Das & Pecht, 2011)will modify both the chemical fingerprint and the quantity of 1,3,5-cycloheptatriene of the electronic component allowing the identification of the counterfeited product before jeopardizing more complex electronic systems.

Conclusions

From this study, the authors demonstrated a viable method for identifying VOC signatures of electronic components utilizing SPME and GCxGC/EI-TOF-MS. The high sensitivity of this sampling method allowed for the identification of hundreds of potential VOC markers for any given electronic component. The methodology exhibited the possibility of differentiating electronic components that vary in their manufacturing, countries of origin, and production dates, based on their VOC signatures. It is possible that other VOC markers could be distinguished by further optimizing the methods outlined above in order to capture more indicative VOC markers for additional electronic components.

Table 3 outlined multiple VOC markers that were consistently identified in each sample group. These significant VOCs could serve as chemical fingerprints for future research focused on identifying VOC markers present in such devices. 1,3,5-cycloheptatriene was identified as a common significant VOC present in the 14-pin, 16-bit microcontrollers and 16 GB microSD here studied. Aging and surface area of the electronic component were identified as critical parameters affecting the final VOCs and their quantity, especially for 1,3,5-cycloheptatriene. Therefore, further work should be related to comparing these findings to counterfeited products to evaluate the differences in terms of significant VOC markers and quantity of 1,3,5-cycloheptatriene as a function of aging, under virgin and expected normal use conditions.

Table 3. Significant VOCs having consistent retention times.

VOC	Sample Group	Retention Time Range (s)	Average Peak Area (un)	Peak Area Standard Deviation (un)
1,3-dimethyl benzene	Microchip Technology	626-632	3.7E+05	2.0E+05
1,3,5-cycloheptatriene	Microchip Technology	496-522	5.3E+05	5.2E+05
Phenol	Texas Instruments	836-840	7.7E+05	2.4E+05
1,1'-(1,2-cyclobutanediyl)bis-, trans-benzene	Texas Instruments	1682-1686	2.9E+05	7.6E+04
Benzaldehyde	Texas Instruments	846-850	3.1E+05	1.1E+05
Hexanal	Texas Instruments	546-550	1.1E+05	4.7E+04
1,3-dimethyl-benzene	Texas Instruments	628-632	2.4E+05	9.0E+04
1,3,5-cycloheptatriene	Texas Instruments	498-502	5.6E+05	2.4E+05
Hexamethylene diacrylate	SanDisk	1492-1496	7.9E+06	2.2E+05
4-acetyl- morpholine	SanDisk	1180-1184	1.3E+06	4.4E+05
2,3-dihydro-5-methyl-furan	SanDisk	370-376	6.5E+06	2.9E+06
1,6-Hexanediol	SanDisk	1062-1068	6.5E+06	1.9E+06
2,2,4-trimethyl-3-hydroxy-, isobutyl ester pentanoic acid	SanDisk	1228-1232	5.5E+06	9.3E+05
1,3,5-Cycloheptatriene	SanDisk	496-514	2.9E+06	1.4E+06
2-methyl-, 1-(1,1-dimethylethyl)-2-methyl-1,3-propanediyl ester propanoic acid	SanDisk	1430-1432	6.6E+06	2.0E+06
2,4-Di-tert-butylphenol	SanDisk	1390-1394	2.6E+06	1.1E+06
Phenol	SanDisk	838-842	6.5E+06	4.0E+06
4-(methylthio)- benzaldehyde	SanDisk	1678-1682	7.6E+05	4.6E+05
butyl dodecanoate	SanDisk	1582-1586	7.3E+05	3.5E+05
1,2-benzene-dicarboxylic acid, bis(2-methylpropyl) ester	SanDisk	1732-1736	2.5E+06	1.5E+06
1,2,3,5-Tetramethyl-benzene, 2-oxime-	SanDisk	1426-1430	1.0E+06	4.2E+05
Tetrahydropyrrolo[2,1-c] [1,4] oxazin-4-one	SanDisk	1392-1396	2.4E+06	7.6E+05
Tetracosamethyl-cyclododeca- siloxane	SanDisk	1952-1956	2.0E+05	6.8E+04
N,N,N- Triethylamine	SanDisk	354-368	2.5E+06	1.6E+06
2,4,6-trimethyl- benzoic acid	SanDisk	1356-1362	4.2E+06	2.9E+06
2,4,6-trimethyl- benzophenone	SanDisk	1736-1740	9.7E+04	5.0E+04
2-(1-methylethyl)- 9H-Thioxanthen-9-one	SanDisk	1970-1978	4.8E+06	3.7E+06
(2-decyldodecyl)-benzene	SanDisk	1460-1472	2.4E+05	1.2E+05
1,2,3-trimethyl-benzene	SanDisk	812-814	8.1E+05	1.5E+05

Acknowledgments

This work was supported by the Indiana Innovation Institute (IN3), Achieving Scientifically Secured User Reassurance in Electronics (ASSURE), Agreement 17002.01, and by a military graduate student research fellowship from the Purdue Military Research Institute.

References

Ahmadi, B., Tavousi, P., Favata, J., Shahbeigi-Roodposhti, P., Pelapur, R., & Shahbazmohamadi, S. (2018). A novel crowdsourcing platform for microelectronics counterfeit defect detection. *Microelectronics Reliability*, *88-90*(July), 48-53. https://doi.org/10.1016/j.microrel.2018.07.107

Brasseur, C., Dekeirsschieter, J., Schotsmans, E. M. J., de Koning, S., Wilson, A. S., Haubruge, E., & Focant, J. F. (2012). Comprehensive two-dimensional gas chromatography-time-of-flight mass spectrometry for the forensic study of cadaveric volatile organic compounds released in soil by buried decaying pig carcasses. *Journal of Chromatography A*, *1255*, 163-170. https://doi.org/10.1016/j.chroma.2012.03.048

Brüggemann, M., Karu, E., & Hoffmann, T. (2016). Critical assessment of ionization patterns and applications of ambient desorption/ionization mass spectrometry using FAPA-MS. *Journal of Mass Spectrometry*, *51*(2), 141-149. https://doi.org/10.1002/jms.3733

Chen, Z. P., Zhang, S. J., & Zhang, L. (2014). Research on identifying and avoiding counterfeit electronic components. *Applied Mechanics and Materials*, *509*, 223-230. https://doi.org/10.4028/www.scientific.net/AMM.509.223

DeGreeff, L. E., Cerreta, M., & Rispoli, M. (2017). Feasibility of Canine Detection of Mass Storage Devices: A Study of Volatile Organic Compounds Emanating from Electronic Devices Using Solid Phase Microextraction. *Journal of Forensic Sciences*, *62*(6), 1613-1616. https://doi.org/10.1111/1556-4029.13472

Gansier, J., Lucyshyn, W., & Rigiliano, J. (2013). Addressing Counterfeit Parts in the DoD Supply Chain. *Tenth Annual Acquisition Research Symposium Logistics Management*. https://dair.nps.edu/bitstream/123456789/1886/1/SYM-LM-13-062.pdf

Gordin, A., & Amirav, A. (2000). SnifProbe: New method and device for vapor and gas sampling. *Journal of Chromatography A*, *903*(1-2), 155-172. https://doi.org/10.1016/S0021-9673(00)00877-3

Hillman, R. J. (2011). DoD Supply Chain: Preliminary Observations Indicate That Counterfeit Electronic Parts Can Be Found on Internet Purchasing Platforms Statement of. *U.S. Government Accountability Office - GAO*. https://apps.dtic.mil/sti/citations/ADA551825

Huang, H., Boyer, A., & Ben Dhia, S. (2015). Electronic counterfeit detection based on the measurement of electromagnetic fingerprint. *Microelectronics Reliability*, *55*(9-10), 2050-2054. https://doi.org/10.1016/j.microrel.2015.07.008

Livingston, H. C. (2010). Securing the DOD Supply Chain from the Risks of Counterfeit Electronic Components. *BAE Systems*, 1–6. https://www.erai.com/CustomUploads/ca/wp/2010_1_Securing_the_DOD_Supply_Chain_from_the_Risks_of_Counterfeit_Electronic_Components.pdf

Microchip Technology Incorporated. (2009). *Datasheet: 20-Pin General Purpose , 16-Bit Flash Microcontrollers PIC24F04KA201 Family*. http://ww1.microchip.com/downloads/en/devicedoc/30009937c.pdf

Mura, G., Murru, R., & Martines, G. (2020). Analysis of counterfeit electronics. *Microelectronics Reliability*, *114*(June), 113793. https://doi.org/10.1016/j.microrel.2020.113793

Pawliszyn, J. (2012). Theory of Solid-Phase Microextraction. *Handbook of Solid Phase Microextraction*. Elsevier Inc. https://doi.org/10.1016/B978-0-12-416017-0.00002-4

Pecht, M., & Tiku, S. (2006). Electronic manufacturing and consumers confront a rising tide of counterfeit electronics. *IEEE Spectrum*, *May*, 37-42. https://doi.org/10.1109/MSPEC.2006.1628506

Petel, G. (2014). Mitigating Counterfeit Electronic Parts Risk: What Epa'S Buy American Checklist Can Teach Dod. *Public Contract Law Journal*, *43*(3), 507-525. https://search.proquest.com/docview/1526285395?accountid=13360&rfr_id=info%3Axri%2Fsid%3Aprimo%0Ahttp://ezproxy.msu.edu/login?url=https://search.proquest.com/docview/1526285395?accountid=12598%0Ahttp://za2uf4ps7f.search.serialssolution.com/?ctx_ver=Z39.88

Pfeuffer, K. P., Caldwell, J., Shelley, J. T., Ray, S. J., & Hieftje, G. M. (2014). Detection of counterfeit electronic components through ambient mass spectrometry and chemometrics. *Analyst*, *139*(18), 4505-4511. https://doi.org/10.1039/c4an01071j

Prebihalo, S. E., Berrier, K. L., Freye, C. E., Bahaghighat, H. D., Moore, N. R., Pinkerton, D. K., & Synovec, R. E. (2018). Multidimensional Gas Chromatography: Advances in Instrumentation, Chemometrics, and Applications. *Analytical Chemistry*, *90*(1) 505-532. American Chemical Society. https://doi.org/10.1021/acs.analchem.7b04226

Reddy, C., & Nelson, R. (2013). Using Comprehensive Two-Dimensional Gas Chromatography to the Explore the Geochemistry of the Santa Barbara Oil Seeps. *United States Department of Energy*. https://doi.org/10.2172/1070069

SanDisk. (2019). *Datasheet: SanDisk Ultra ® microSDXC ™ & microSDHC ™ UHS-I Cards*. https://documents.westerndigital.com/content/dam/doc-library/en_us/assets/public/sandisk/product/memory-cards/ultra-uhs-i-microsd/data-sheet-ultra-uhs-i-microsd.pdf

Semiconductor Industry Association SIA. (2011). *Detecting and Removing Counterfeit Semiconductors in the U . S . Supply Chain Manufacturing and Reliability of*

Genuine Semiconductors vs . Counterfeits Require Government Purchase from Authorized Sources. https://www.semiconductors.org/wp-content/uploads/2018/06/ACTF-Whitepaper-Counterfeit-One-Pager-Final.pdf

Sood, B., Das, D., & Pecht, M. (2011). Screening for counterfeit electronic parts. *Journal of Materials Science: Materials in Electronics*, *22*(10), 1511-1522. https://doi.org/10.1007/s10854-011-0500-0

Stadler, S., Stefanuto, P. H., Byer, J. D., Brokl, M., Forbes, S., & Focant, J. F. (2012). Analysis of synthetic canine training aids by comprehensive two-dimensional gas chromatography-time of flight mass spectrometry. *Journal of Chromatography A*, *1255*, 202-206. https://doi.org/10.1016/j.chroma.2012.04.001

Sugawara, T. (2007). *Crosslinkable Resin Composition and Resin Formed Body Produced Therefrom* (Patent No. US007,273,915 B2). U.S Patent and Trademark Office. https://patents.google.com/patent/EP1655343A4/en

Sullivan, B. A., & Wilson, J. M. (2017). An empirical examination of product counterfeiting crime impacting the U.S. military. *Trends in Organized Crime*, *20*(3-4), 316-337. https://doi.org/10.1007/s12117-017-9306-7

Texas Instruments. (2004). *MSP430x2xx Family User's Guide*, *38*(3). www.ti.com

U.S. Department of Commerce. (2010). *Defense Industrial Base Assessment: Counterfeit Electronics*. http://bis.doc.gov/defenseindustrialbaseprograms/

United States Government Accountability Office. (2016). *Counterfeit parts: DOD needs to improve reporting and oversight to reduce supply chain risk* (Issue February). https://www.gao.gov/assets/680/675227.pdf

Biographies

JOSEPH CACCIATORE is an officer in the United States Marine Corps. He obtained his MS degree in engineering technology as a member of the Purdue Military Research Institute. His research interests include using two-dimensional gas chromatography to aide in ensuring electronics authenticity for applications in the Department of Defense. Mr. Cacciatore may be reached at joseph.cacciatore@usmc.mil

PETR VOZKA is an assistant professor in the Department of Chemistry and Biochemistry at California State University, Los Angeles. Dr. Vozka's research interest focuses on the characterization of complex chemical mixtures via state-of-the-art techniques, such as two-dimensional gas chromatography and high-resolution mass spectrometry. Dr. Vozka may be reached at pvozka@calstatela.edu

LOUIS EDWARDS CACERES-MARTINEZ is a graduate student in the School of Engineering Technology at Purdue University. He obtained both his MS and BS degrees in mechanical engineering from Universidad Nacional de Colombia. His research interests include the development of high-performance renewable blendstock fuels via two-dimensional gas chromatography and mass spectrometry, biomass conversion, and thermal modeling. Mr. Caceres-Martinez may be reached at lcaceres@purdue.edu

ALI DANESHKHAH is a research associate working in the Backman Lab at the Biomedical Engineering Department of Northwestern University. Dr. Daneshkhah's research areas of interest include super-resolution microscopy, biomarker discovery, clinical and translational research, VOC analysis, and image processing. Dr. Daneshkhah may be reached at alid@northwestern.edu

MANGILAL AGARWAL is a professor of mechanical and energy engineering at Indiana University—Purdue University Indianapolis (IUPUI). Dr. Agarwal's research is focused on the design and development of nano-sensors using a canine-inspired model for medical screening and diagnostics. Additionally, Dr. Agarwal's research group works on the design and fabrication of flexible energy devices and systems. Dr. Agarwal may be reached at agarwal@iupui.edu

GOZDEM KILAZ is an associate professor in the School of Engineering Technology and Aviation and Transportation Technology (by courtesy) at Purdue University. She holds BS, MS, and PhD degrees in chemical engineering. Currently, she serves as the Director of the Fuel Laboratory of Renewable Engineering (FLORE). Her research is focused on characterization and synthesis, ASTM certifications, and the safety and sustainability of transportation liquid fuels via state-of-the-art analytical techniques, such as two-dimensional gas chromatography and mass spectrometry. Dr. Kilaz may be reached at gkilaz@purdue.edu

ERIC DIETZ is Director of the Purdue Homeland Security Institute, Director of the Purdue Military Research Institute and a professor in the Computer and Information Technology Department at Purdue University. Dr. Dietz's research interests include measurement and optimization of emergency response, homeland security and defense, energy security, and engaging veterans in higher education. As the Director of the Purdue Homeland Security Institute, Dr. Dietz organizes interdisciplinary homeland security research including increasing the impact of Purdue's research on society. Dr. Dietz may be reached at jedietz@purdue.edu

FEASIBILITY OF HYDROGEN STORAGE

Kassie Mobley, Texas A&M University; Steve Thompson, Texas A&M University; Behbood Zoghi, Texas A&M University

Abstract

There is a growing demand for cleaner energy in the United States and across the globe, and a move away from a reliance on fossil fuels. According to the U.S. Energy Information Administration (EIA, n.d.), our sources of energy include petroleum (35%), Natural Gas (34%), renewable energy (12%), coal (10%), and nuclear (9%). While natural gas is relatively clean burning, it still will need to be replaced in an effort to meet net-zero carbon demands. This discussion has been the catalyst for energy providers to determine if hydrogen can be the energy source of the future. In this current study, the authors compared natural gas to hydrogen in terms of storage medium availability and gas properties.

The analysis provided the data needed to quantitatively model the gases and show technical and economic feasibility. Currently, natural gas is stored underground in domal salt, bedded salt, depleted reservoirs, and depleted aquifers; infrastructure and business models are in place for the transmission and use of natural gas. Because the thermodynamic properties of natural gas and hydrogen differ, it takes three times the amount of hydrogen to provide the same amount of energy as natural gas. This means a greater cost for the operator and, consequently, the consumer. Simulation modeling of gas properties, expert interviews, and qualitative and quantitative analyses revealed that an initial return on investment was estimated to be 160.8%/year for hydrogen gas storage.

It was recommended that the storage of natural gas be continued as well as the investment in research and development of hydrogen, which should include the technical feasibility of storage mediums other than domal salt along with infrastructure and transmission needs and the cost of moving from natural gas to hydrogen. Expertise in the fossil fuel industry paves the way for a cleaner future for the energy industry.

Definition of Terms

The net size of caverns is expressed in units of millions of barrels (mmbbls). The net size defines the amount of void space inside the cavern. Total capacity is defined as the total volume of gas needed to fill the cavern to maximum pressure. Total capacity is equal to the sum of base gas plus working gas. Base gas is defined as the volume of gas that must remain in the cavern to maintain minimum pressure gradients. Working gas is defined as the volume of gas within a cavern that can be withdrawn or injected into the cavern. Working gas is profitable. It is sold in units of energy (millions of btu per standard cubic feet, MMbtu/scf).

Background/Introduction

Storage of energy is a crucial factor in the business of selling energy. The fossil fuel portion of the energy industry provides the most power to consumers. According to the Energy Information Agency (EIA), fossil fuels make up 60% of energy provided. Currently, natural gas is the most environmentally friendly fossil fuel and is used to power electrical plants, homes, and various other industries. Natural gas storage has provided, on average, 3464 bcf of gas between 2016-2020 (EIA). This is what helps to supply the energy demand in the U.S.; and 34% of this supply is provided by natural gas (EIA). This is done by storing natural gas in domal salt, bedded salt, depleted reservoirs, and depleted aquifers.

Underground storage has been a business for many years. Today, depleted reservoirs, depleted aquifers, bedded salt, and domal salt are used to store natural gas. Domal salt, however, is also used to store other energy carriers including oil, liquid natural gas (LNG), and hydrogen. Prior to storing each energy carrier, a cavern must be created within the salt dome. This is done by drilling a well into the salt formation, followed by leaching of the cavern using freshwater that reacts with the salt to create brine. The brine is withdrawn by injecting the energy carrier into the cavern, forcing the brine to the surface; the brine is then stored in brine ponds and/or saltwater disposal wells. The result of this process is the creation of a void in which the energy carrier (oil, natural gas, LNG, hydrogen, etc.) can be stored.

Hydrogen is the lightest element in the periodic table. It has a density 1/8 that of natural gas. On a molecular level, a hydrogen molecule is four times smaller than a natural gas molecule. Additionally, hydrogen has a higher compressibility factor compared to natural gas (greater than 1). This means that, as hydrogen is compressed, it will occupy space less efficiently than natural gas. This is important because pressure increases with depth. Thus, hydrogen will store less efficiently than natural gas. In other words, three times more hydrogen is needed to provide the same amount of energy as natural gas. The thermodynamic properties of each gas define these major differences and help to determine how each gas will behave. The thermodynamic properties for hydrogen and natural gas are listed below (Minas, 2021).

Hydrogen

- Gas Density: 0.00531 lb_m/ft^3
- Atomic Radius: 25pm
- Dynamic Viscosity: 5.86E-06 lb_m/ft * 3
- Compressibility Factor: 1.001

- Net Heating Value: 51586.212Btu/lb_m, 273.943Btu/lb_m
- Joule-Thompson Coefficient: -0.00349 °F/psia
- Thermal Conductivity: 0.101Btu/h * ft * °F
- Isobaric Heat Capacity: 3.411Btu/lb_m * °F
- Flammability Rangy by Volume: 4 - 74% (Note: pm = 1 x 10^{-12} m).

Natural Gas

- Gas Density: 0.0424lb_m/ft^3
- Atomic Radius: 95pm
- Dynamic Viscosity: 7.24E-06lb_m/ft * 3
- Compressibility Factor: 0.998
- Net Heating Value: 21525.407Btu/lb_m, 912.034Btu/lb_m
- Joule-Thompson Coefficient: 0.058°F/psia
- Thermal Conductivity: 0.0189Btu/h * ft * °F
- Isobaric Heat Capacity: 0.528Btu/lb_m * °F
- Flammability Rangy by Volume: 5 - 15% (Note: pm = 1 x 10^{-12} m).

The compositions of each gas were assumed to be 100% methane for natural gas and 100% hydrogen for hydrogen gas. These numbers are integral to the understanding of the behaviors of natural gas and hydrogen gas.

Hydrogen Production

Hydrogen does not exist freely in the atmosphere; it is always found with other elements such as water (H_2O) and methane (CH_4). Hydrogen production is the process of separating hydrogen from other elements. Each type of production is given a color. The color represents the method used to produce the hydrogen as well as the environmental impact. The most common method is steam methane reforming (SMR) coupled with a water-gas shift reaction (WGS), while the least common method is the utilization of electrolysis, a process that uses electricity to split water into hydrogen and oxygen. The term grey hydrogen indicates SMR plus WGS with a release of CO_2 into the atmosphere. Blue hydrogen indicates SMR plus WGS with the sequestration and storage of CO_2. Green hydrogen indicates the use of electrolysis powered by renewable resources to produce hydrogen that has no harmful byproduct. Table 2 shows the differences among the types of hydrogen production.

Table 2. Types of hydrogen production.

	Grey Hydrogen	Blue Hydrogen	Green Hydrogen
Method	SMR+WGS	SMR+WGS	Electrolysis
Chemical Reaction	$CH_4+2H_2O=CO+4H_2$	$CH_4+2H_2O=CO+4H_2$	$H_2O-->O_2+H_2$
Byproduct	CO_2 to atmosphere	CO_2 sequestered and stored	No harmful byproduct

They type of hydrogen production correlates to profitability, as each has a different cost. According to Earth.org (Shin, 2020), green hydrogen costs $3.00-$7.50 per kg, while grey hydrogen costs $0.90-$3.20 per kg. The aspect of cost must also consider the cost of developing a salt cavern for storage. According to Lord, Kobos and Borns (2014), the cost of developing a salt cavern is just over $60 million, which translates to $1.60 per kg. The cost of hydrogen and the cost of storage development explain why the most widely used hydrogen production method is grey followed by blue, with green as the least used method.

Literature Review

The storage of gases underground has been researched extensively. The interest in underground hydrogen storage has increased as the discussion around cleaner energy takes hold. There have been various publications that detail the design and transport criteria, risks, and design considerations. Tarkowski (2019) detailed the various types of storage mediums to consider for hydrogen storage pros and cons for each type of storage. In that publication, the author proposed salt cavern storage as the dominant storage medium since it is proven for hydrogen. The use of depleted reservoirs, aquifers, and bedded salt pose much greater risk, given the properties of hydrogen.

The risk associated with hydrocarbon storage in bedded salt is discussed at length in a study by Daemen, Du, Jing, Yang and Zhang (2013) in which the authors concluded that there is increased leakage risk with bedded salt as compared to domal salt or other storage mediums. In an article by Amid, Mignard and Wilkinson (2016), the authors evaluated the storage of hydrogen in depleted reservoirs and depleted aquifers, comparing natural gas storage in terms of working gas, base gas, and technical considerations. Ozarslan (2012) discussed the proven ability to store hydrogen in domal salt caverns. In another study, Panfilov (2016) detailed the threats surrounding the behavior of hydrogen within a storage medium and incorporated a risk discussion regarding the use of a pipeline to transport the hydrogen.

The determination was that there was a significant difference between natural gas reaction with formation compared to hydrogen in a depleted reservoir and depleted aquifer, including chemical reactions with surrounding formation, gas loss to the formation, and potential leakage rate. In addition, the author discussed pipeline infrastructure as a means of transporting hydrogen and concluded that a better understanding of metallurgical constraints and leakage potential were needed. Minas and Skaug (2021) discussed salt cavern design for hydrogen where the emphasis was on the properties of hydrogen and the resulting effect on metallurgical design for the construction of salt cavern wells for hydrogen storage. In an article by Nieland (2008), the author compared the salt cavern design among hydrogen, natural gas, and compressed air in order to determine the amount of working gas versus base gas for each type of gas stored.

The author concluded with a comparison of which type of gas had the greatest amount of working gas per storage capacity; natural gas had the greatest amount of working gas followed by compressed air with hydrogen having the least amount of working gas.

Hydrogen Transportation Considerations

An aspect of hydrogen storage that must be considered in the transportation of the gas. The capability to store hydrogen is just as important as the capability to transport the hydrogen to market. Cowell, Kurz and Vignal (2020) provide insight into the metallurgical challenges as well as a decrease in pipeline deliverability that would occur as a result of hydrogen being introduced into the pipeline; the greater the amount of hydrogen, the greater the effects on metallurgy and deliverability. Additionally, the Hydrogen and Fuel Cell Technologies Office (2021) reviewed the current state of pure hydrogen pipelines and determined that a conversion of natural gas hydrogen pipelines to pure hydrogen pipelines would be extremely challenging. Such a project would require more research and understanding before projects of such magnitude could become a reality.

There are multiple opportunities for growing the use of hydrogen in the energy sector. These uses and their financial implications have been studied and published. Weeda and Ball (2016) discussed reliance on fossil fuels being unsustainable when considering predicted population growth from now through 2050. The solution for this is the increased use of renewable resources, specifically hydrogen for fueling cars and providing power through electrolysis to enhance the overall power provided by renewable resources. Ballotpedia (2021) reviewed the history of environmental policies in the U.S. from the 1970s to the present. In this 50-year history, there had been incremental increases in renewable resources as part of tax incentives. In more recent years, there has been a change from tax incentives being the only driver to enforceable environmental regulation driving implementation of renewable resources as well.

Nguyen and Schwartz (2021) provided a financial model of the potential market for using the excess power from wind turbines to produce hydrogen through electrolysis and store it in salt caverns. In turn, the hydrogen could be used for power generation during periods of inactive wind activity. Frey, Morisani-Zechmeister and Simone (2021) modeled the use of a hydrogen-natural gas blend to meet the demand for cleaner energy. In that article, the authors also compared salt cavern storage for natural gas as a baseline for comparing natural gas alone versus a blend of hydrogen and natural gas. Frey et al. (2021) also discussed transportation constraints and how these could affect the use of a hydrogen -natural gas blend.

Methodology

In this current project, the authors conducted both qualitative and quantitative research in order to determine the feasibility of underground hydrogen storage. The qualitative portion consisted of research, conferences, workshops, interviews, and interpretive analysis. The quantitative method used was modeling. The purpose of the modeling was to demonstrate the items listed below and use the results to complete the interpretive analysis portion of the qualitative methodology. This was done by researching and analyzing the methods of hydrogen production, infrastructure requirements, metallurgical considerations, storage mediums (i.e., domal cavern, bedded salt, depleted reservoir, depleted aquifer, etc.,), and ability to convert natural gas storage to hydrogen storage. Finally, the cost associated with hydrogen storage was analyzed and comparative modeling was used to determine hydrogen storage feasibility. Specifically,

1) Volume of hydrogen that can be stored in a cavern at a given pressure and temperature.
2) Volume of natural gas that can be stored in a cavern at a given pressure and temperature.
3) Volume of hydrogen working gas and base gas available at given pressures and temperatures.
4) Volume of natural gas working gas and base gas at given pressures and temperatures.
5) Amount of energy available in natural gas cavern versus hydrogen gas cavern.

Figure 1 shows a broad view of a salt dome with small schematics of leached caverns. Figure 2 shows a basic cavern schematic with the casing shoe labeled. The gas volume is measured by reading pressure on the casing shoe then converting that pressure to a gas volume. The integrity of the cavern depends on operating within the pressure range allowed between base gas (minimum pressure) and maximum capacity (base gas plus working gas). Salt dome caverns vary in size and shape, thus the volume of base gas and working gas will differ. However, the minimum and maximum pressure gradients are the same. The recommended pressure gradients are defined in API 1170 Section 9.1 (American Petroleum Institute).

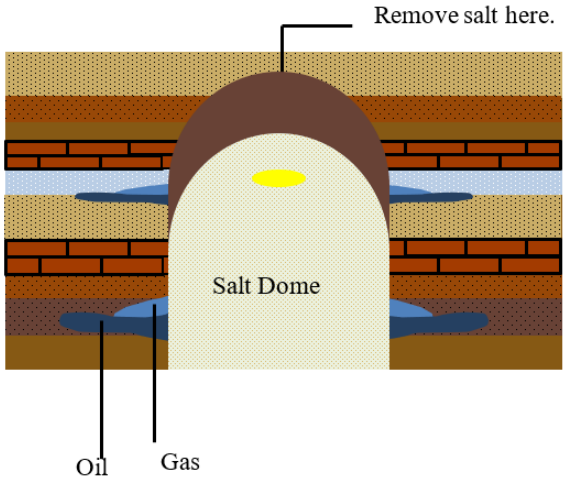

Figure 1. Salt dome.

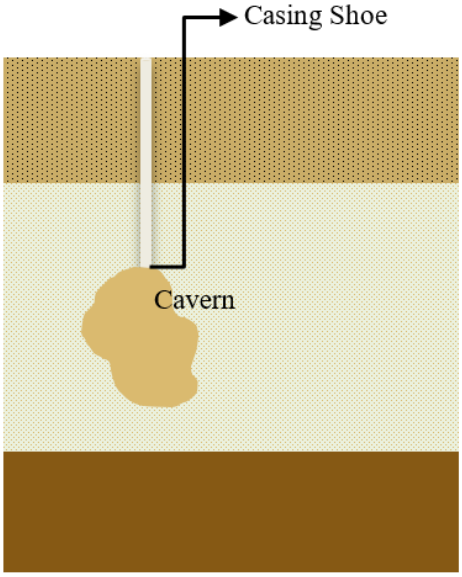

Figure 2. Basic salt dome cavern schematic.

The participants included interviews with subject matter experts as well as assistance with developing the quantitative model. These participants had, collectively, 70 years in the energy industry. The qualitative instruments consisted of research papers, interviews, workshop presentations, conference presentations, and graphical data for interpretive analysis. The quantitative instrument was a data simulation model that allowed for the input of gas properties needed to calculate the amount of gas available in an underground storage cavern given various thermodynamic properties. Gas properties and calculation assumptions were inputted into the simulation model. The model then calculated total gas capacity, working gas capacity, and base gas capacity for the hydrogen gas cavern and natural gas cavern models. The results were collected and inputted into tables and graphs for interpretive analysis of the qualitative methodology.

This procedure was repeated for three different scenarios: shallow-depth cavern, medium-depth cavern, and deep-depth cavern. Each scenario had three iterations for modeling various cavern sizes along with the depths. The scenarios demonstrated the behavioral differences between hydrogen and natural gas at different pressures. This is important for the determination of working gas volumes and, thus, profitability.

Quantitative Data Modeling

The model was based on the formula PV = znRT: where, *P* is pressure; *V* is volume; *z* is the compressibility factor for the given gas; *n* is the amount of gas; *R* is the ideal gas constant; and, *T* is the temperature (in degrees Fahrenheit). There were assumptions built into the model. These assumptions were gas composition, method for calculating the *z* factor, and method for calculating bottom hole pressure (bhp). The model used assumed the AGA8 method for calculating compressibility factor, and *z* as defined in the American Gas Association's Report No. 3. The Cullender-Smith method was used for calculating bottom hole pressure, as described in Natural Gas Reservoir Engineering (Ikoku, 1992). The gas compositions assumed were

- Hydrogen gas composition
- H_2 (hydrogen): 100%
- Natural Gas composition*
- C_1 (methane): 94.920%
- N_2 (nitrogen): 0.285%
- CO_2 (carbon dioxide): 0.966%
- C_2 (ethane): 3.522%
- C_3 (propane) 0.223%

[*Note: In this gas composition, the IC4 (isobutane), NC4 (normal butane), IC5 (isopentane), NC5 (normal pentane), C6 (hexanes), C7 (heptanes), C8 (octanes), and C9 (nonanes) make up 0.084% of the composition. This brings the total to 100%.]

Additional assumptions are listed below. Their purpose is to have an "all else equal" baseline in order to narrow the focus on the difference in gas behavior and their related effects; that is, given that all costs and cavern parameters are equal.

- Transportation
- Pipeline Infrastructure
- Surface Facility Infrastructure
- Market Availability
- Cavern Depths
- Cavern Net Size
- Casing Shoe Depth
- Cavern Roof Depths
- USD Gas Price $3.72/MMBtu (NASDAQ 2021 Natural Gas Cavern Average)

There were three scenarios with three iterations for each scenario. Scenario 1 was the shallowest of the caverns with a casing shoe depth of 2000 feet and a cavern roof depth of 2100 feet, with a total depth of 3500 feet. In Scenario 2, the casing shoe depth was 3000 feet, the cavern roof depth was 3100 feet, and the total cavern depth of the cavern was 4500 feet. In Scenario 3, the casing shoe depth was 4000 feet, the cavern roof was 4100 feet, and the total depth of the cavern was 5500 feet. Each scenario was run with three iterations. The iterations compared cavern size differences at the scenario depths. The net size for iteration one was a 6-million-barrel cavern; iteration two used an 8-million-barrel cavern; and, iteration three used a 10-million-barrel cavern. Table 3 shows the results of these iterations and scenarios. The parameters and assumptions were inputted into the model for both the natural gas composition and hydrogen gas composition assumptions. The resulting calculation yielded total gas capacity, base gas capacity, and working gas capacity in units of billion cubic feet (bcf). Table 4 shows these capacities.

Table 3. Quantitative modeling scenarios and iterations.

Quantitative Modeling Scenarios and Iterations		
Scenario 1		
Casing shoe depth	2000.00	ft
Cavern roof depth	2100.00	ft
Cavern total depth	3500.00	ft
Iteration 1: Net Size = 6 mmbbls		
Iteration 2: Net Size = 8 mmbbls		
Iteration 3: Net Size = 10 mmbbls		
Scenario 2		
Casing shoe depth	3000.00	ft
Cavern roof depth	3100.00	ft
Cavern total depth	4500.00	ft
Iteration 1: Net Size = 6 mmbbls		
Iteration 2: Net Size = 8 mmbbls		
Iteration 3: Net Size = 10 mmbbls		
Scenario 3		
Casing shoe depth	4000.00	ft
Cavern roof depth	4100.00	ft
Cavern total depth	5500.00	ft
Iteration 1: Net Size = 6 mmbbls		
Iteration 2: Net Size = 8 mmbbls		
Iteration 3: Net Size = 10 mmbbls		

The working gas capacities were then converted to millions of btu per standard cubic feet (MMBtu/scf) in order to compare the energy content between natural gas and hydrogen. Table 5 shows the results of the conversion. The conversion formula for bcf to MMBtu is as follows:

- Natural Gas = 1030 btu/scf
- Hydrogen gas = 325 btu/scf
- Therm = 100,000 BTU
- Deka = 10
- Dekatherm = 10*100,000 BTU = 1 million BTU
- 1.030 million btu = MCF of Natural Gas = 1.030 Dekatherms
- Hydrogen = 0.325 million BTU or 0.325 Dekatherm

The results of the model were used in the interpretive analysis of the qualitative portion of the methodology.

Qualitative Interpretive Analysis

The interpretive analysis used working gas capacity differences between natural gas and hydrogen gas. The results of the model showed that there was less working gas in hydrogen gas caverns than natural gas caverns for each iteration of each scenario. Additionally, hydrogen has 1/3 less energy content than natural gas, as shown in the energy content conversion. This means the natural gas profit margin is greater than hydrogen. Figure 3 shows profit for natural gas versus hydrogen, assuming an equal market. The average 2021 market for natural gas was $3.72 MMBtu/scf. A clear difference in profit can be seen from this figure.

In addition to this profit difference, three times more hydrogen is needed to provide the same amount of energy as natural gas. Currently, there is not enough underground storage available to replace natural gas with hydrogen. This is inferred because the only proven underground storage for hydrogen is salt dome caverns, as discussed by a number of authors found in the literature review for this paper. Natural gas is stored in salt dome caverns, bedded salt caverns, depleted reservoirs, and depleted aquifers. This means that, even if the profits were equal, the availability to provide the required energy that is in current demand would not be possible with hydrogen. The underground storage of natural gas is still a necessity. The results of the model require a

Table 4. Quantitative modeling scenarios and iterations results.

Quantitative Modeling Scenarios and Iterations Results			Scenario 1			Scenario 2			Scenario 3		
			6	8	10	6	8	10	6	8	10
Hydrogen	Total	bcf	3.240	4.310	5.390	5.737	7.650	9.560	7.977	10.640	13.295
	Base	bcf	0.883	1.177	1.471	1.631	2.175	2.719	2.358	3.144	3.930
	Working	bcf	2.353	3.137	3.922	4.106	5.474	6.842	5.619	7.492	9.365
Natural Gas	Total	bcf	3.997	5.330	6.662	5.067	9.993	12.491	9.997	13.329	16.661
	Base	bcf	0.961	1.281	1.601	1.888	2.517	3.146	2.890	3.853	4.816
	Working	bcf	3.036	4.049	5.061	5.607	7.476	9.345	7.107	9.476	11.845

Table 5. Working gas to energy content conversion results.

Working Gas to Energy Content Conversion Results (bcf to MMBtu/scf)										
Natural Gas	MMBtu	3.13	4.17	5.21	5.78	7.70	9.63	7.32	9.76	12.20
Hydrogen	MMBtu	0.76	1.02	1.27	1.33	1.78	2.22	1.83	2.43	3.04

return to the assumptions. Specifically, transportation, pipeline infrastructure, and market conditions that would impact the market. If hydrogen gas were to replace natural gas, the additional cost incurred to update current infrastructure to meet the needs of hydrogen would be passed on to the consumer. This would create an even greater profit differential between hydrogen and natural gas, thereby strengthening the results of the original model.

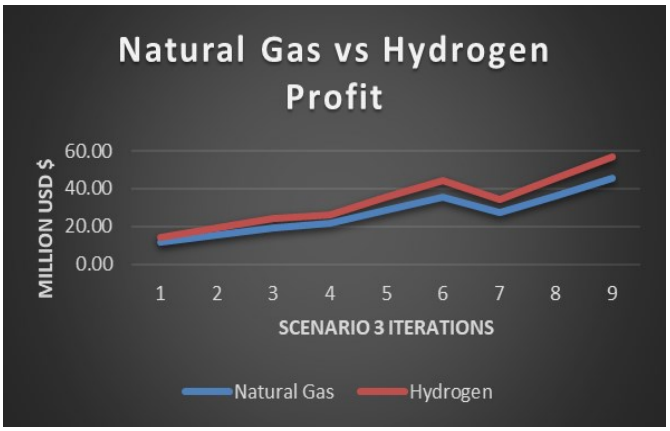

Figure 3. Natural gas vs. hydrogen profit.

Return on Investment

The ROI for this project was compared for hydrogen gas storage and natural gas storage. There were two cases reflected for ROI. The values reflected for ROI considered a previously developed domal salt storage cavern storage facility that included four storage caverns. Table 6 shows the yearly maintenance cost for this project estimated the cost of one mechanical integrity test (MIT), yearly subsidence report, yearly inventory logging, yearly maintenance logging, and yearly regulatory fees totaling $990,000. Further costs included facility maintenance and pipeline maintenance, each with a yearly cost of $6,250,000—yielding a new total cost of $12,500,000. Noble inhouse labor was estimated to be $2,000,000 per year to support the planning and overall execution of the above stated O&M work. This cost included salary and overall benefits package, bringing the project total to $15,490,000.

For this project, the numbers reflected assumed that hydrogen gas had the same market value as natural gas storage, which was $3.72 MMBtu/scf, according to NASDAQ 2021 averages. It was further assumed that all working gas was sold for each cavern. Table 7 shows a comparison of net return on investment of hydrogen and natural gas. In the case of hydrogen gas storage, and considering investment costs of $15,490,000 and a net return on investment of $24,910,000, an initial return on investment each year was estimated to be 160.8%. In the case of natural gas storage, and considering investment cost of $15,490,000 and a net return on investment of $103,140,000, an initial return on investment each year was estimated to be 665.8%.

Table 6. Cost of investment summary.

Cost of Investment	
Cavern Mechanical Integrity Test (MIT)	$120,000
Cavern Subsidence Reports	$50,000
Cavern Inventory Logging	$150,000
Regulatory Fees	$20,000
Cavern Maintenance Logging	$650,000
Facility Maintenance	$6,250,000
Pipeline Maintenance and Inspection	$6,250,000
Labor	$2,000,000
Total:	$15,490,000

Table 7. Net return on investment summary.

Net Return on Investment	Hydrogen (MMBtu/scf)	
Cavern 1	0.76	$2,840,000
Cavern 2	1.27	$4,740,000
Cavern 3	2.22	$8,270,000
Cavern 4	2.43	$9,060,000
	Total:	$24,910,000
Net Return on Investment	Natural Gas (MMBtu/scf)	
Cavern 1	3.13	$11,630,000
Cavern 2	5.21	$19,390,000
Cavern 3	9.63	$35,810,000
Cavern 4	9.76	$36,310,000
	Total:	$103,140,000

Recommendations and Conclusion

It can be seen in the results from this study that ROI was significantly higher for natural gas storage than hydrogen gas storage. This ROI did come with the assumption that the market for hydrogen and natural gas were equivalent and the infrastructure needs were equivalent. Additionally, the storage medium utilized was domal salt caverns since it was the only proven method for hydrogen gas. Given the assumptions, it is recommended that natural gas storage continue to be stored and sold for energy needs. It is also recommended that a percentage of revenue be dedicated to research into capital development and costs associated with

1. Facility Infrastructure
2. Pipeline Infrastructure
3. Depleted Reservoir Storage
4. Hydrogen production technology

The storage of hydrogen gas for the purpose of replacing natural gas will not be feasible financially or technically until it is cheaper to produce green hydrogen, the infrastructure is more thoroughly understood, and there are more available methods of storage. These cumulative factors must align in order for hydrogen gas storage to be profitable for an operator. In this project, the authors modeled natural gas and hydrogen gas at various depths and various cavern sizes. From this modeling, working gas, which was shown to have a greater capacity with natural gas than hydrogen in each scenario, was calculated. In addition, the modeling showed that the energy content for hydrogen was 1/3 less than the energy content of natural gas. This proved that more hydrogen is needed to provide the same amount of energy as natural gas. Thus, more storage space would be needed.

From this project, the authors concluded that the only storage medium technically viable for hydrogen gas was domal salt. Thus, the authors recommend that more sound storage spaces for hydrogen be developed. Additional recommendations include investing in the future by taking a percentage of revenue and putting it toward research of infrastructure as well as green hydrogen production. Research funding is vital, as there is a responsibility on the operator to invest in the future of energy that incorporates a higher percentage of renewable resources than is currently part of the energy business. For the energy future to change, holding costs down is vital to the overall feasibility. These factors along with an estimated rate of return of 685.8% for natural gas compared to 160.8% for hydrogen lead to the recommendation that continuing to invest in the storage of natural gas while investing in a hydrogen future is in the best interest of the operator and the end user.

References

AGA. Report No. 8, Compressibility Factors of Natural Gas and Other Related Hydrocarbon Gases, 2nd and 3rd Editions, American Gas Association, Washington, D.C., 1992, 1994, 2017.

Amid, A., Mignard, D., & Wilkinson, M. (2016). Seasonal storage of hydrogen in a depleted reservoir. *International Journal of Hydrogen Energy, 41*(12), 5549-5558. https://doi.org/10.1016/j.ijhydene.2016.02.036

Ballotpedia. (2021, November 5). Environmental policy of the United States. *Ballotpedia*. https://ballotpedia.org/Historical_energy_policy_in_the_United_States

Cowell, M., Kurz, R., & Vignal, M., (2020). Hydrogen in pipelines. *Pipeline Technology Journal, 3*, 64-72. https://www.pipeline-journal.net/journal/pipeline-technology-journal-32020

Daemen, J. J. K., Du, C., Jing, W., Yang, C., & Zhang, G. (2013). Analysis of major risks associated with hydrocarbon storage caverns in bedded salt. *Reliability Engineering & System Safety, 113*, 94-111. https://doi.org/10.1016/j.ress.2012.12.017

EIA (n,d.). U.S. Energy Information Administration, *Weekly Natural Gas Storage Report*. https://www.eia.gov/naturalgas/reports.php#/T202

Frey, F., Morisani-Zechmeister, A., & Simone, A. (2021). Preparing for hydrogen future—constraints and alternatives for hydrogen storage. *SMRI Fall 2021 Technical Conference*. Galveston, Texas.

Hydrogen and Fuel Cell Technologies Office. (2021). *Hydrogen Pipelines*. Office of Energy Efficiency & Renewable Energy. https://www.energy.gov/eere/fuelcells/Hydrogen-pipelines

Ikoku, C. U. (1992). *Natural gas reservoir engineering*. Krieger Publishing Company.

Lord, A. S., Kobos, P. H., & Borns, D. J. (2014). Geologic storage of hydrogen: Scaling up to meet city transportation demands. *International Journal of Hydrogen Energy, 39*(28), 15570-15582.

Minas, S. (2021). *Hydrogen salt cavern design*. SMRI Fall 2021 Technical Conference, Galveston, Texas.

Nieland, J. D. (2008). Salt cavern thermodynamics-comparison between hydrogen, natural Gas, and air storage. *SMRI Fall 2008 Technical Conference*. Rapid City, South Dakota.

Nguyen, D., & Schwartz, B. (2021). Techno-economic analysis of enhanced performance large-scale wind power generation using underground hydrogen storage. *SMRI Fall 2021 Technical Conference*. Galveston, Texas.

Ozarslan, A. (2012). Large-scale hydrogen energy storage in salt caverns. *International Journal of Hydrogen Energy, 37(19)*, 14265-14277. https://doi.org/10.1016/j.ijhydene.2012.07.111

Panfilov, M. (2016). 4-Underground and pipeline hydrogen storage. In Woodhead Publishing Series in Energy. Basile, A., Gupta, R.B., & Veziroglu, N. (Eds.), *Compendium of Hydrogen Energy* (pp. 91-115). Woodhead Publishing. https://doi.org/10.1016/B978-1-78242-362-1.00004-3

Shin, J. (2020, September 17). What is green hydrogen. Earth.org. https://earth.org/green-hydrogen/

Tarkowski, R. (2019). Underground storage: characteristics and prospects. *Renewable and Sustainable Energy Reviews, 105*, 86-94. https://doi.org/10.1016/j.rser.2019.01.051

Weeda, M., & Ball, M. (2016). 11-The hydrogen economy – vision or reality? In Woodhead Publishing Series in Energy. Ball, M., Basile, A., & Veziroglu, N. (Eds.), *Compendium of Hydrogen Energy* (pp. 237-266). Woodhead Publishing. https://doi.org/10.1016/B978-1-78242-364-5.00011-7

Biographies

KASSIE MOBLEY is the Senior Petroleum Geologist at Enbridge. She obtained her Bachelor of Science degree in geology and Master of Science degree in engineering technical management from Texas A&M University. Ms. Mobley may be reached at kass.mob@tamu.edu

STEPEHN THOMPSON holds a PhD in chemistry from the University of Dundee, Scotland. Dr. Thompson has 30 years' industry experience, with a focus on technology, processes, operational methods, and quality associated with electronics, procurement, and distribution. He is a veteran industry professional with expertise in semiconductor processes, equipment fabrication, operations, supplier management, and quality. Dr. Thompson has a proven record of driving world-class performance for global operations, quality, and products through immediate improvement actions, defect prevention, model-based decision making, and organizational commitment to performance management systems. He is an excellent team builder, analyst, and problem solver, and an expert in implementing solutions in large, complex, and time-critical organizations. Dr. Thompson's corporate career includes senior management experience in Europe, Asia, and North America. Dr. Thompson has lived in the United States, Denmark, Switzerland, and the United Kingdom, and traveled extensively throughout Europe and Asia. Dr. Thompson may be reached at swthompson@tamu.edu

BEHBOOD ZOGHI is the Victor H. Thompson chair professor of Electronics System Engineering Technology at Texas A&M. He directs the RFID/Sensor Lab and the new online professional Master of Engineering in Technical Management program. A member of the Texas A&M University faculty for 30 years, he has distinguished himself as a teacher, writer, and researcher, and has been honored for his teaching excellence by the College and the Texas A&M University Association of Former Students. Ben's academic and professional degrees are from Texas A&M (PhD), The Ohio State University (MSEE), and Seattle University (BSEE). Dr. Zoghi may be reached at zoghi@tamu.edu

INSTRUCTIONS FOR AUTHORS: MANUSCRIPT FORMATTING REQUIREMENTS

The INTERNATIONAL JOURNAL OF MODERN ENGINEERING is an online/print publication designed for Engineering, Engineering Technology, and Industrial Technology professionals. All submissions to this journal, submission of manuscripts, peer-reviews of submitted documents, requested editing changes, notification of acceptance or rejection, and final publication of accepted manuscripts will be handled electronically. The only exception is the submission of separate high-quality image files that are too large to send electronically.

All manuscript submissions must be prepared in Microsoft Word (.doc or .docx) and contain all figures, images and/or pictures embedded where you want them and appropriately captioned. Also included here is a summary of the formatting instructions. You should, however, review the sample Word document on our website (http://ijme.us/formatting_guidelines/) for details on how to correctly format your manuscript. The editorial staff reserves the right to edit and reformat any submitted document in order to meet publication standards of the journal.

The references included in the References section of your manuscript must follow APA-formatting guidelines. In order to help you, the sample Word document also includes numerous examples of how to format a variety of scenarios. Keep in mind that an incorrectly formatted manuscript will be returned to you, a delay that may cause it (if accepted) to be moved to a subsequent issue of the journal.

1. **Word Document Page Setup:** Two columns with ¼" spacing between columns; top of page = ¾"; bottom of page = 1" (from the top of the footer to bottom of page); left margin = ¾"; right margin = ¾".

2. **Paper Title:** Centered at the top of the first page with a 22-point Times New Roman (Bold), small-caps font.

3. **Page Breaks:** Do not use page breaks.

4. **Figures, Tables, and Equations:** All figures, tables, and equations must be placed immediately after the first paragraph in which they are introduced. And, each must be introduced. For example: "Figure 1 shows the operation of supercapacitors." "The speed of light can be determined using Equation 4:"

5. **More on Tables and Figures:** Center table captions above each table; center figure captions below each figure. Use 9-point Times New Roman (TNR) font. Italicize the words for table and figure, as well as their respective numbers; the remaining information in the caption is not italicized and followed by a period—e.g., "*Table 1*. Number of research universities in the state." or "*Figure 5*. Cross-sectional aerial map of the forested area."

6. **Figures with Multiple Images:** If any given figure includes multiple images, do NOT group them; they must be placed individually and have individual minor captions using, "(a)" "(b)" etc. Again, use 9-point TNR.

7. **Equations:** Each equation must be numbered, placed in numerical order within the document, and introduced—as noted in item #4.

8. **Tables, Graphs, and Flowcharts:** All tables, graphs, and flowcharts must be created directly in Word; tables must be enclosed on all sides. The use of color and/or highlighting is acceptable and encouraged, if it provides clarity for the reader.

9. **Textboxes:** Do not use text boxes anywhere in the document. For example, table/figure captions must be regular text and not attached in any way to their tables or images.

10. **Body Fonts:** Use 10-point TNR for body text throughout (1/8" paragraph indention); indent all new paragraphs as per the images shown below; do not use tabs anywhere in the document; 9-point TNR for author names/affiliations under the paper title; 16-point TNR for major section titles; 14-point TNR for minor section titles.

11. **Personal Pronouns:** Do not use personal pronouns (e.g., "we" "our" etc.).

12. **Section Numbering:** Do not use section numbering of any kind.

13. **Headers and Footers:** Do not use either.

14. **References in the Abstract:** Do NOT include any references in the Abstract.

15. **In-Text Referencing:** For the first occurrence of a given reference, list all authors—last names only—up to seven (7); if more than seven, use "et al." after the seventh author. For a second citation of the same reference—assuming that it has three or more authors—add "et al." after the third author. Again, see the *sample Word document* and the *formatting guide for references* for specifics.

16. **More on In-Text References:** If you include a reference on any table, figure, or equation that was not created or originally published by one or more authors on your manuscript, you may not republish it without the expressed, written consent of the publishing author(s). The same holds true for name-brand products.

17. **End-of-Document References Section:** List all references in alphabetical order using the last name of the first author—last name first, followed by a comma and the author's initials. Do not use retrieval dates for websites.

18. **Author Biographies:** Include biographies and current email addresses for each author at the end of the document.

19. **Page Limit:** Manuscripts should not be more than 15 pages (single-spaced, 2-column format, 10-point TNR font).

20. **Page Numbering:** Do not use page numbers.

21. **Publication Charges:** Manuscripts accepted for publication are subject to mandatory publication charges.

22. **Copyright Agreement:** A copyright transfer agreement form must be signed by all authors on a given manuscript and submitted by the corresponding author before that manuscript will be published. Two versions of the form will be sent with your manuscript's acceptance email.

    Only one form is required. Do not submit both forms!

    The form named "paper" must be hand-signed by each author. The other form, "electronic," does not require hand signatures and may be filled out by the corresponding author, as long as he/she receives written permission from all authors to have him/her sign on their behalf.

23. **Submissions:** All manuscripts and required files and forms must be submitted electronically to Dr. Philip D. Weinsier, manuscript editor, at philipw@bgsu.edu.

24. **Published Deadlines:** Manuscripts may be submitted at any time during the year, irrespective of published deadlines, and the editor will automatically have your manuscript reviewed for the next-available issue of the journal. Published deadlines are intended as "target" dates for submitting new manuscripts as well as revised documents. Assuming that all other submission conditions have been met, and that there is space available in the associated issue, your manuscript will be published in that issue if the submission process—including payment of publication fees—has been completed by the posted deadline for that issue.

    Missing a deadline generally only means that your manuscript may be held for a subsequent issue of the journal. However, conditions exist under which a given manuscript may be rejected. Always check with the editor to be sure. Also, if you do not complete the submission process (including all required revisions) within 12 months of the original submission of your manuscript, your manuscript may be rejected or it may have to begin the entire review process anew.

CUTTING EDGE JOURNAL OF RESEARCH AND INNOVATION IN ENGINEERING

Print ISSN: 2152-4157
Online ISSN: 2152-4165

www.ijeri.org

www.iajc.org

INTERNATIONAL JOURNAL OF ENGINEERING RESEARCH AND INNOVATION

ABOUT IJERI:

- IJERI is the second official journal of the International Association of Journals and Conferences (IAJC).
- IJERI is a high-quality, independent journal steered by a distinguished board of directors and supported by an international review board representing many well-known universities, colleges, and corporations in the U.S. and abroad.
- IJERI has an impact factor of **1.58**, placing it among an elite group of most-cited engineering journals worldwide.

OTHER IAJC JOURNALS:

- The International Journal of Modern Engineering (IJME) For more information visit www.ijme.us
- The Technology Interface International Journal (TIIJ) For more information visit www.tiij.org

IJERI SUBMISSIONS:

- Manuscripts should be sent electronically to the manuscript editor, Dr. Philip Weinsier, at philipw@bgsu.edu.

  For submission guidelines visit www.ijeri.org/submissions

TO JOIN THE REVIEW BOARD:

- Contact the chair of the International Review Board, Dr. Philip Weinsier, at philipw@bgsu.edu.

  For more information visit www.ijeri.org/editorial

INDEXING ORGANIZATIONS:

- IJERI is currently indexed by 16 agencies. For a complete listing, please visit us at www.ijeri.org.

Contact us:

Mark Rajai, Ph.D.

Editor-in-Chief
California State University-Northridge
College of Engineering and Computer Science
Room: JD 4510
Northridge, CA 91330
Office: (818) 677-5003
Email: mrajai@csun.edu

www.tiij.org

www.ijme.us

THE LEADING JOURNAL OF ENGINEERING, APPLIED SCIENCE AND TECHNOLOGY

The latest impact factor (IF) calculation (Google Scholar method) for IJME of 3.0 moves it even higher in its march towards the top 10 engineering journals.

IJME IS THE OFFICAL AND FLAGSHIP JOURNAL OF THE INTERNATIONAL ASSOCATION OF JOURNALS AND CONFERENCE (IAJC)
www.iajc.org

The International Journal of Modern Engineering (IJME) is a highly-selective, peer-reviewed journal covering topics that appeal to a broad readership of various branches of engineering and related technologies. IJME is steered by the IAJC distinguished board of directors and is supported by an international review board consisting of prominent individuals representing many well-known universities, colleges, and corporations in the United States and abroad.

IJME Contact Information

General questions or inquiries about sponsorship of the journal should be directed to:

Mark Rajai, Ph.D.
Editor-in-Chief
Office: (818) 677-5003
Email: editor@ijme.us
Department of Manufacturing Systems Engineering & Management
California State University-Northridge
18111 Nordhoff St.
Northridge, CA 91330